

## Objective Eulerian coherent structures

Mattia Serra and George Haller

Citation: **Chaos** **26**, 053110 (2016); doi: 10.1063/1.4951720

View online: <http://dx.doi.org/10.1063/1.4951720>

View Table of Contents: <http://scitation.aip.org/content/aip/journal/chaos/26/5?ver=pdfcov>

Published by the AIP Publishing

---

### Articles you may be interested in

[Traveling waves in Hall-magnetohydrodynamics and the ion-acoustic shock structure](#)

*Phys. Plasmas* **21**, 022109 (2014); 10.1063/1.4862035

[On the numerical solution of a two dimensional elliptic-parabolic equation](#)

*AIP Conf. Proc.* **1479**, 606 (2012); 10.1063/1.4756205

[Computing Lagrangian coherent structures from their variational theory](#)

*Chaos* **22**, 013128 (2012); 10.1063/1.3690153

[An application of solvable structures to classical and nonclassical similarity solutions](#)

*J. Math. Phys.* **42**, 3714 (2001); 10.1063/1.1368845

[Painlevé–Calogero correspondence revisited](#)

*J. Math. Phys.* **42**, 1443 (2001); 10.1063/1.1348025

---



# Objective Eulerian coherent structures

Mattia Serra<sup>a)</sup> and George Haller<sup>b)</sup>

Institute for Mechanical Systems, ETH Zürich, Leonhardstrasse 21, 8092 Zurich, Switzerland

(Received 7 December 2015; accepted 10 May 2016; published online 25 May 2016)

We define objective Eulerian Coherent Structures (OECSSs) in two-dimensional, non-autonomous dynamical systems as the instantaneously most influential material curves. Specifically, OECSSs are stationary curves of the averaged instantaneous material stretching-rate or material shearing-rate functionals. From these objective (frame-invariant) variational principles, we obtain explicit differential equations for hyperbolic, elliptic, and parabolic OECSSs. As an illustration, we compute OECSSs in an unsteady ocean velocity data set. In comparison to structures suggested by other common Eulerian diagnostic tools, we find OECSSs to be the correct short-term cores of observed trajectory deformation patterns. *Published by AIP Publishing.* [<http://dx.doi.org/10.1063/1.4951720>]

**Short-term variability in material structures is often seen as significant in unsteady flows. Such variability is of prime interest in many fields ranging from flow control to environmental assessment, where quick operational decisions need to be made. Existing methods for the identification of the instantaneously most influential structures for deformation patterns, however, are often frame-dependent and lack a rigorous mathematical foundation. This, in turn, limits the reliability of the results they provide. Here, we develop a rigorous global variational theory of objective Eulerian Coherent Structures (OECSSs), which uncover the correct instantaneous skeletons of the flow, in a frame-invariant fashion.**

## I. INTRODUCTION

Coherent structures behind material pattern formation in unsteady flows have received considerable attention (see, e.g., Refs. 4, 28, and 30, for reviews). Among other mathematical advances (Refs. 1, 5, 13, 26, and 29), variational techniques have been developed to identify Lagrangian Coherent Structures (LCSs), the most influential cores of material deformation, in experimental and numerical velocity data (Refs. 10–12, 16, and 18).

Specifically, initial positions of hyperbolic LCSs (generalized stable and unstable manifolds), elliptic LCSs (generalized KAM tori) and parabolic LCSs (generalized jet cores) are now readily computable as solutions of differential equations defined over the initial configuration of a system.<sup>17</sup> Later positions of these LCSs are then obtained by advecting their initial positions under the flow map. By the objectivity (frame-invariance) of their underlying variational principles, variational LCSs transform properly under coordinate changes  $x \mapsto \tilde{x}$  of the form

$$x = Q(t)\tilde{x} + b(t), \quad (1)$$

<sup>a)</sup>Electronic mail: serram@ethz.ch

<sup>b)</sup>Author to whom correspondence should be addressed. Electronic mail: georgehaller@ethz.ch

where  $Q(t)$  is an arbitrary proper orthogonal tensor family generating time-dependent rotations, and  $b(t)$  is an arbitrary vector family introducing time-dependent translations of the frame.<sup>32</sup>

All LCSs, however, are intrinsically tied to a specific finite time interval over which they exert their influence on nearby trajectories. This influence is an integrated one, filtering out short-term anomalies in the flow. Yet short-term variability in material structures is often seen as significant in highly unsteady flows, explaining the popularity of Eulerian (i.e., instantaneous velocity-based) diagnostic fields in fluid dynamics (see, e.g., Refs. 15, 21, and 6 for reviews).

Eulerian diagnostics generally highlight features of the velocity field in a given frame of reference. Most studies of flows, nevertheless, would ideally want to understand, forecast, or control the evolution and mixing of *material trajectories*, as well as the transport of the physical properties they carry. Indeed, the motivation for each commonly used Eulerian diagnostic is invariably grounded in the desire to understand particle motion over short time scales. Yet the approximations and heuristics employed in deriving these diagnostics, as well as the expectation for simply implementable results, tends to change the original focus of these approaches from material features to the analysis of frame-dependent velocity features.

Even short-term identifications of *material* coherence, however, must be frame-invariant by definition. This is because material coherent structures are composed of trajectories, which do not depend on coordinates and hence must transform properly under (1) from the frame of one observer to the other's. If a proposed coherent structure criterion labels different material sets as coherent in different frames, then it either lacks a proper physical foundation, or its physical foundation is implemented through erroneous mathematics. Either way, the criterion cannot be used reliably in nowcasting or real-time decision-making under unsteady flow conditions.<sup>29</sup>

The few available objective Eulerian coherent structure diagnostics include that of Tabor and Klapper,<sup>31</sup> who consider a point elliptic (i.e., part of a vortex) if the vorticity

expressed on the basis of the rate-of-strain eigenvectors dominates strain (see also Refs. 23 and 24). Another objective Eulerian technique is the recent global approach<sup>19</sup> to rotationally coherent vortices. Identified as an outermost closed level sets of the instantaneous vorticity deviation (IVD) from the spatial mean vorticity, IVD-based vortex boundaries are objective, short-term limits of closed curves obtained from a global Lagrangian rotational coherence principle.

Here, we introduce a more general approach to Objective Eulerian Coherent Structures (OECSSs) in two dimensions. We effectively seek these structures as short-term limits of LCSs. In contrast to Ref. 19, we use the stretching-based variational LCS theories in taking this limit. As a consequence, we obtain a broader class of OECSSs that includes elliptic (vortex-type), hyperbolic (stretching or contracting), and parabolic (jet-type) structures.

We give an explicit parametrization of all these types of OECSSs as solutions of autonomous ordinary differential equations (ODEs). Our approach is global, eliminating the shortcomings of local structure identification schemes noted in Ref. 25. All OECSSs are computable without dependence on any chosen time scale. They are also objective, depending solely on the invariants of the rate-of-strain tensor, i.e., the symmetric part of the velocity gradient.

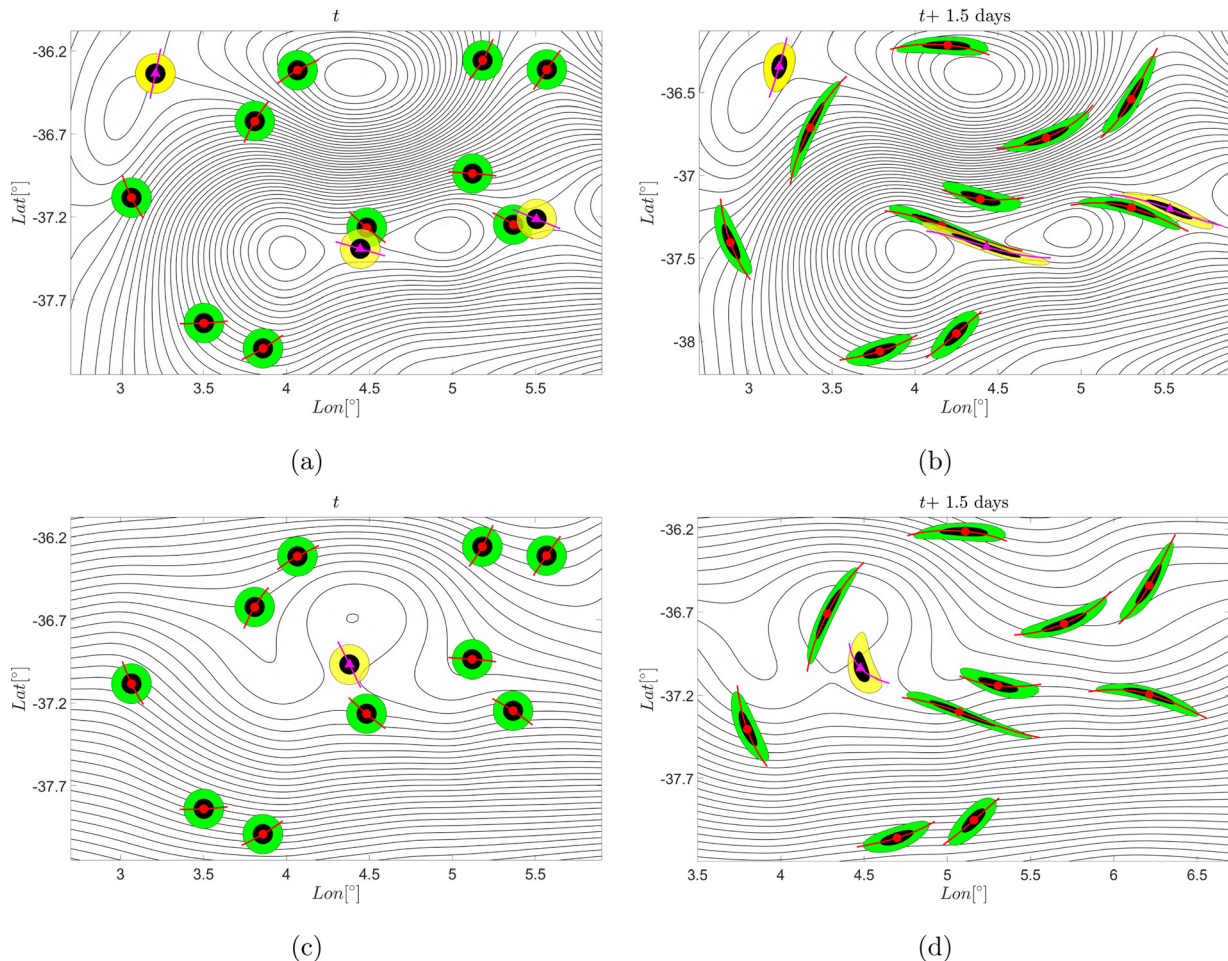
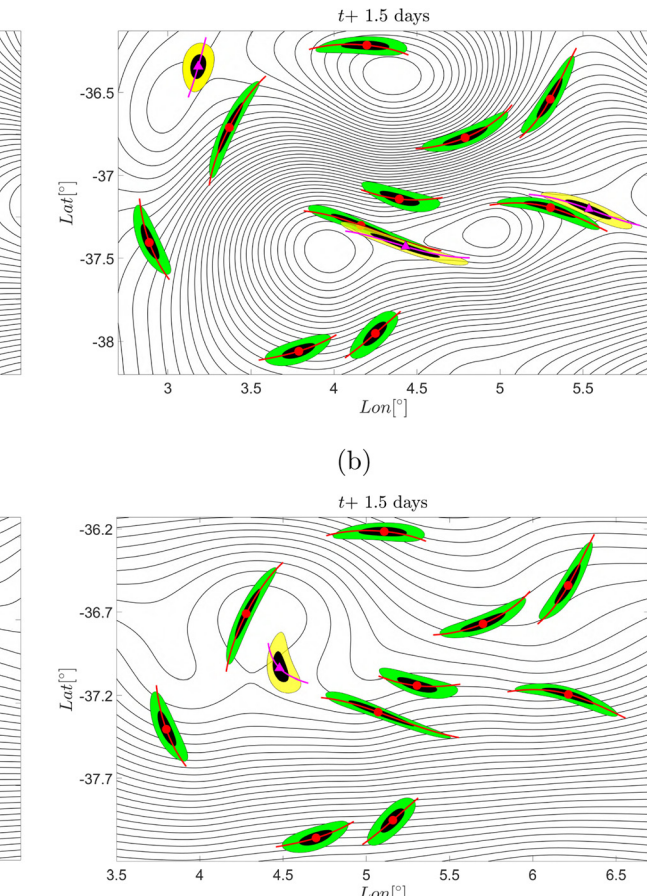


FIG. 1. (a) Attracting hyperbolic OECSSs (red) with their cores (red dots) and classic saddle-type stagnation points (magenta triangles) with their corresponding unstable directions (magenta), overlaid on streamlines. (b) Advected image of the hyperbolic OECSSs and classic saddle-type stagnation points after 1.5 days, and their effect on nearby particles. (c) and (d) Same phenomenon shown in (a) and (b), seen from an observer moving with constant longitudinal velocity ( $-0.6^\circ/\text{day}$ ) relative to the one used in (a) and (b).

As an illustration of the results we derive here, Fig. 1 compares hyperbolic OECSSs and the classic frame-dependent saddle-type stagnation points computed on an ocean velocity data (see Section VIII for more details). The effect of those structures on nearby particles and the instantaneous streamlines are also shown. In particular, Figs. 1(a) and 1(b) show the attracting hyperbolic OECSSs (red) with their cores (red dots) and the saddle-type stagnation points (magenta triangles) with their unstable directions (magenta) at the initial time, and after short-term advection. In contrast, Figs. 1(c) and 1(d) show the same features observed from a frame translating in the longitudinal direction with constant speed ( $-0.6^\circ/\text{day}$ ), relative to the one used in Figs. 1(a) and 1(b).

This example highlights two important facts. First, frame-dependent diagnostics, such as instantaneous stagnation points, are unsuitable for the self-consistent identification of coherent structures: the three saddle-type stagnation points detected by one observer (Figs. 1(a) and 1(b)) disappear when the same phenomenon is analyzed by another observer in a moving frame (Figs. 1(c) and 1(d)). In this second frame, a single saddle-type stagnation point emerges at an unrelated location and induces no notable material stretching.



Second, and more important, hyperbolic OECSSs capture an actual saddle-type material behavior in several locations with no stagnation points in their vicinities. Similar conclusions hold for elliptic and parabolic OECSSs (cf. Section VIII). Based on this example, we expect OECSSs to be useful in a number of physical situations where reliable nowcasting, or short-term forecasting, and control of material transport are critical.

We develop a theoretical foundation for our global variational OECSS theory in Sections III–VI. Readers interested mainly on a practical implementation of the automated OECSSs detection may proceed directly to Section VII, which gives a summary of the results along with the corresponding numerical schemes. In Section VIII, we perform the OECSSs detection in a two-dimensional ocean velocity data obtained from satellite altimetry. We show that the variational OECSSs outperform traditional Eulerian diagnostics in locating the skeletons of short-term material deformation.

## II. SET-UP AND NOTATION

Consider the two-dimensional non-autonomous dynamical system

$$\dot{x} = v(x, t), \quad (2)$$

with a twice continuously differentiable velocity field  $v(x, t)$  defined over an open flow domain  $U \in \mathbb{R}^2$ , over a time interval  $t \in [a, b]$ . We recall the customary velocity gradient decomposition

$$\nabla v(x, t) = S(x, t) + W(x, t),$$

with the rate-of-strain tensor  $S = \frac{1}{2}(\nabla v + \nabla v^T)$  and the spin tensor  $W = \frac{1}{2}(\nabla v - \nabla v^T)$ . By our assumptions,  $S(x, t)$  and  $W(x, t)$  are continuously differentiable in  $x$  and  $t$ . Under an observer change (1), the new rate-of-strain tensor and the new spin tensor are obtained in the form

$$\begin{aligned} \tilde{S}(\tilde{x}, t) &= Q^T(t)S(x, t)Q(t), \\ \tilde{W}(\tilde{x}, t) &= Q^T(t)W(x, t)Q(t) - Q^T(t)\dot{Q}(t), \end{aligned} \quad (3)$$

as shown in classic texts on continuum mechanics (see, e.g., Ref. 32). Therefore, the rate-of-strain tensor is objective, as it transforms as a linear operator, whereas the spin tensor is not the objective.

The eigenvalues  $s_i(x, t)$  and eigenvectors  $e_i(x, t)$  of  $S(x, t)$  are defined, indexed, and oriented here through the relationship

$$\begin{aligned} Se_i &= s_i e_i, \quad |e_i| = 1, \quad i = 1, 2; \quad s_1 \leq s_2, \quad e_2 = Re_1, \\ R &:= \begin{pmatrix} 0 & -1 \\ 1 & 0 \end{pmatrix}. \end{aligned} \quad (4)$$

We also recall that the rate of length change for an infinitesimal material element vector  $\ell$  based at  $x$  is

$$\frac{1}{2} \frac{d}{dt} |\ell|^2 = \langle \ell, S(x, t) \ell \rangle. \quad (5)$$

A further key relationship between the flow map  $F_{t_0}^t : x_0 \mapsto x(t; t_0, x_0)$  of (2) and  $S(x, t)$  is obtained by considering the right Cauchy–Green strain tensor,

$$C_{t_0}^t = [\nabla F_{t_0}^t]^T \nabla F_{t_0}^t, \quad (6)$$

whose temporal Taylor expansion around the initial time can be computed as

$$C_{t_0}^t(x_0) = I + 2S(x_0, t_0)(t - t_0) + \mathcal{O}(|t - t_0|^2), \quad (7)$$

(cf. eq. A1, Appendix A). In other words, for small enough times, the leading order Lagrangian deformation is governed by the Eulerian rate-of-strain tensor. This observation enables us to consider the Eulerian coherent structures as short-time limits of Lagrangian coherent structures.

Although OECSSs are instantaneous limits of LCSs, these two families of coherent structures are not interchangeable. Specifically, OECSSs are free from any time scale and reveal the instantaneous centerpieces of deformation patterns. LCSs computed over short times, instead, are tied to small but finite time scales which are abundant in general unsteady flows. Furthermore, short-term LCSs have weak signatures since the Cauchy–Green tensor is close to the identity (cf. Eq. (7)). By contrast, OECSSs are computed from the rate-of-strain tensor which is generally far from the identity tensor, and hence has rich features.

## III. OBJECTIVE DEFORMATION RATES

At an arbitrary time  $t$ , consider a smooth curve  $\gamma \subset U$ , parametrized in the form  $x(s)$  by its arclength  $s \in [0, \sigma]$ . Then the unit vectors  $x'(s)$  and  $n(s) = R \frac{x'(s)}{|x'(s)|}$ , with the rotation matrix  $R$  appearing in (4), define a local tangent and a local normal to  $\gamma$  at the point  $x(s)$ . The following definition fixes the notions of instantaneous material shear rate and material stretching rate along  $\gamma$ . While these quantities are intuitively clear, we also give their detailed derivation in Appendix A as first-order terms in the temporal Taylor expansion of the analogous finite-time Lagrangian shear and stretching measures (cf. Ref. 17).

**Definition 1.** Material deformation rates at time  $t$  along a material curve  $\gamma$  with arclength parametrization  $x(s)$ :

(1) *Material stretching rate*:

$$\dot{q}(x, x', t) = \frac{\langle x', S(x, t)x' \rangle}{\langle x', x' \rangle}$$

(2) *Material shear rate*:

$$\dot{p}(x, x', t) = \frac{\langle x', [S(x, t)R - RS(x, t)]x' \rangle}{\langle x', x' \rangle}. \quad (8)$$

Physically,  $\dot{q}$  gives the instantaneous tangential stretching rate along  $\gamma$ , while  $\dot{p}$  represents twice the rotation rate due to shear of an initially normal perturbation to  $\gamma$ . The objectivity of these Eulerian deformation rate measures follows from (3) together with the commutation between an arbitrary planar rotation  $Q(t)$  and the  $90^\circ$  rotation  $R$ .

#### IV. VARIATIONAL PRINCIPLES FOR OECSS

Using the Eulerian deformation rates introduced in Definition 1, we now define the averaged stretch- and shear-rate functionals over an arbitrary curve  $\gamma$  at time  $t$ :

**Definition 2.** At time  $t$  along the material curve  $\gamma$ :

(1) *The averaged material stretch-rate is*

$$\dot{Q}_t(\gamma) = \frac{1}{\sigma} \int_{\gamma} \dot{q}(x(s), x'(s), t) ds. \quad (9)$$

(2) *The averaged material shear-rate is*

$$\dot{P}_t(\gamma) = \frac{1}{\sigma} \int_{\gamma} \dot{p}(x(s), x'(s), t) ds. \quad (10)$$

By smooth dependence of  $v(x, t)$  on  $x$  and  $t$ , one expects to see  $\mathcal{O}(\epsilon)$  variability in the average material stretch- or shear-rates across an  $\mathcal{O}(\epsilon)$  strip of material lines surrounding  $\gamma$ . Exceptional choices of  $\gamma$ , however, defy this trend, displaying only an  $\mathcal{O}(\epsilon^2)$  variability of  $\dot{Q}_t(\gamma)$  or  $\dot{P}_t(\gamma)$  in  $\mathcal{O}(\epsilon)$  strips around  $\gamma$ . Such  $\gamma$  curves will act as centerpieces of coherence in the material stretch-rate or material shear-rate fields.

This lack of leading order variability in the averaged stretch-rate or shear-rate along  $\gamma$  is equivalent to the vanishing of the first variation of the functional  $\dot{Q}_t$  or  $\dot{P}_t$  on  $\gamma$ . The former case occurs on the instantaneous vortex boundaries with no short-term unevenness in their tangential deformation (no short-term filamentation). Figure 2 shows a material curve  $\gamma$  (black) with a surrounding material belt  $\gamma + \epsilon h$  (red) at the current time  $t$  and at a later time  $t + \tau$ . The evolution is shown for a typical material belt and for an atypical (coherent) belt. Specifically, in the limit of  $\tau \rightarrow 0$ , Fig. 2 illustrates the meaning of a stationary curve of an averaged stretch rate.

The latter case arises for curves that are cores of short-term shear-type deformation (instantaneous jets) or short-term hyperbolic stretching (instantaneous hyperbolic structures). We formalize these definitions below, using the time derivatives of the corresponding global variational LCS definitions reviewed in Ref. 17.

**Definition 3.** At time  $t$

(1) *A closed curve  $\gamma$  is an elliptic OECSS if it is a stationary curve of the averaged stretch-rate functional  $\dot{Q}$ , i.e.,*

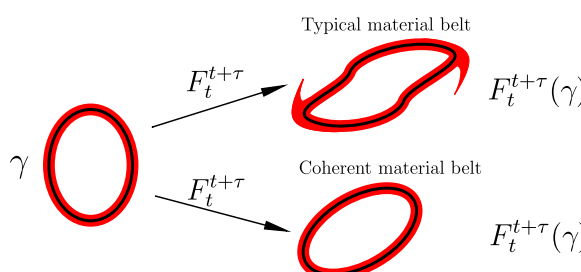


FIG. 2. A closed material curve  $\gamma$  (black), at time  $t$ , is advected by the flow into its later position  $F_t^{t+\tau}(\gamma)$ ,  $0 < \tau \ll 1$ . The advected curve remains coherent in the limit of  $\tau \rightarrow 0$  if an initially uniform material belt (red) around it shows no leading-order variations in the material-line averaged stretch rate  $\dot{Q}_r$ .

$$\delta \dot{Q}_t(\gamma) = 0. \quad (11)$$

(2) *A curve  $\gamma$  is a shearless OECSS if it is a stationary curve of the averaged shear-rate functional  $\dot{P}_t$ , i.e.,*

$$\delta \dot{P}_t(\gamma) = 0. \quad (12)$$

The variational problems outlined in (11) and (12) are equivalent to the weak Euler-Lagrange equations

$$\delta \dot{Q}_t(\gamma) = \frac{1}{\sigma} [\langle \partial_{x'} \dot{q}, h \rangle]_0^\sigma + \frac{1}{\sigma} \int_0^\sigma \left[ \partial_x \dot{q} - \frac{d}{ds} \partial_{x'} \dot{q} \right] h ds = 0, \quad (13)$$

$$\delta \dot{P}_t(\gamma) = \frac{1}{\sigma} [\langle \partial_{x'} \dot{p}, h \rangle]_0^\sigma + \frac{1}{\sigma} \int_0^\sigma \left[ \partial_x \dot{p} - \frac{d}{ds} \partial_{x'} \dot{p} \right] h ds = 0, \quad (14)$$

with  $h(s)$  denoting small perturbations to the curve  $\gamma$ . We discuss below the solutions of Equations (13) and (14), building on similar ideas developed for LCSs (Refs. 10 and 18). This approach will lead to explicit solutions of (11) and (12), and enable a further partitioning of shearless OECSSs into hyperbolic and parabolic OECSSs.

#### V. ELLIPTIC OECSS

By Definition 3, an elliptic OECSS is a closed curve, and hence its small perturbation  $h(s)$  used in calculating the first variation of  $\dot{Q}_t$  along  $\gamma$  is also periodic with the same period  $\sigma$ . As a consequence, the first bracketed term in (13) vanishes. Then, by the fundamental lemma of the calculus of variations, Equation (11) becomes equivalent to the classic Euler–Lagrange equations

$$\partial_x \dot{q} - \frac{d}{ds} \partial_{x'} \dot{q} = 0. \quad (15)$$

The detailed form of this equation is similar to the Euler–Lagrange equation derived in Ref. 18 for elliptic LCSs (stationary curves of the averaged, finite-time tangential stretch along the material curve  $\gamma$ ). The only difference in the present context is that the expression for  $\dot{q}$  has no square root, and contains the rate-of-strain tensor  $S(x, t)$  instead of the Cauchy–Green strain tensor  $C_{t_0}^t(x_0)$  defined in (6). Therefore, following the procedure similar to the one adopted in Ref. 18, we obtain the following full characterization of elliptic OECSSs.

**Theorem 1.** *Elliptic OECSSs at time  $t$  coincide with limit cycles of the differential equation family*

$$\frac{dx}{ds} = \chi_{\mu}^{\pm}(x, t), \quad \chi_{\mu}^{\pm} = \sqrt{\frac{s_2 - \mu}{s_2 - s_1}} e_1 \pm \sqrt{\frac{\mu - s_1}{s_2 - s_1}} e_2, \quad (16)$$

defined for any parameter value  $\mu \in \mathbb{R}$  on the set

$$U_{\mu} := \{x \in U : s_1 \neq s_2, s_1 \leq \mu \leq s_2\}.$$

Along any elliptic OECSS obtained for a given value of  $\mu$ , the material stretching rate at time  $t$  is pointwise constant and equal to  $\dot{q} \equiv \mu$ .

The right-hand side of the differential equation (16) is only locally a vector field in  $U_{\mu}$ , because the rate-of-strain

eigenvector fields  $e_i$  are generally not globally orientable in  $U$ . Local orientability of  $\chi_\mu^\pm(x, t)$  in  $U_\mu$ , however, is always possible. This makes the trajectories, and specifically the limit cycles, of the differential equation (16) well defined. Due to the lack of a well-defined orientation for eigenvector fields, it is a-priori unknown which one of the  $\chi_\mu^\pm$  fields can have limit cycles. Therefore, both vector fields should be checked for limit cycles.

Along limit cycles obtained for  $\mu = 0$ , we have  $\dot{q} \equiv 0$ . Such elliptic OECSs are perfectly coherent in the Eulerian sense, exhibiting uniformly zero pointwise material stretching rate. The direction field  $\chi_\mu^\pm$  ceases to be well-defined at locations of repeated rate-of-strain eigenvalues ( $s_1 = s_2$ ). Following the terminology used in Ref. 18, we refer to such locations as *singularities* of the tensor field  $S(\cdot, t)$ . An appropriate extension of Poincaré's classic index theory implies that there are at least two singularities of  $S$  in the interior of any limit cycle of  $\chi_\mu^\pm$ . This in turn leads to an automated detection algorithm that applies equally to elliptic OECSs. We refer to Ref. 22 for a detailed discussion of this algorithm for elliptic LCSs.

By their hyperbolicity (i.e., strict attraction or repulsion of nearby trajectories of the vector field  $\chi_\mu^\pm$ ), elliptic OECSs are robust with respect to moderate errors and uncertainties in the underlying velocity field  $v(x, t)$ . Figure 3(a) summarizes the main properties of perfectly coherent elliptic OECSs. Detailed discussions on the numerical detection of limit cycles of directions fields can be found in Refs. 18 and 22 for LCS. These can be directly applied here after replacing  $C_{t_0}^t(x_0)$  with  $S(x, t)$ .

Under changes in the parameter  $\mu$ , limit cycles of  $\chi_\mu^\pm$  arise in continuous, non-intersecting families (see Appendix B). An *Eulerian vortex boundary* can then be defined as the

outermost member of such an elliptic OECS family. Given the objectivity of each member of such a limit cycle family, Eulerian vortex boundaries defined in this fashion are also objective.

Figure 3(b) shows such a family and its outermost member in a flow example analyzed in more detail in Section VIII. A nested OECS family often signals a nearby coherent Lagrangian vortex boundary, as is the case in Fig. 3(b). Just as in the case of elliptic LCSs,<sup>18</sup> solutions of the variational principle (11) can also be viewed as closed null-geodesics of a Lorentzian metric family

$$g_\mu(u, u) = \langle u, S_\mu u \rangle, \quad S_\mu(x, t) = [S(x, t) - \mu I], \quad (17)$$

which has a metric signature  $(-, +)$ .<sup>2</sup> The tensor family  $S_\mu$  denotes a generalized rate-of-strain tensor and the parameter  $\mu$  denotes the instantaneous tangential stretching rate on  $\gamma$ . In this context, locations of repeated eigenvalues of  $S(x, t)$  are singularities for the metric  $g_\mu$  which becomes degenerate at these points (cf. Fig. 3).

## VI. SHEARLESS OECS

By Definition 3, a shearless OECS at time  $t$  is a stationary curve of the averaged shear-rate functional  $\dot{P}_t$ , and hence satisfies the weak Euler–Lagrange equation (14). We can pass to the strong form of these Euler–Lagrange equation if the first bracketed term in (14) vanishes for the class of admissible perturbations  $h(s)$  applied to the parametrization  $x(s)$  of the stationary curve  $\gamma$  we seek.

Following the procedure developed in Ref. 10 for an elliptic LCS, we find the following class of admissible perturbations for which the boundary term  $\langle \partial_x \dot{p}, h \rangle$  in (14) vanishes:

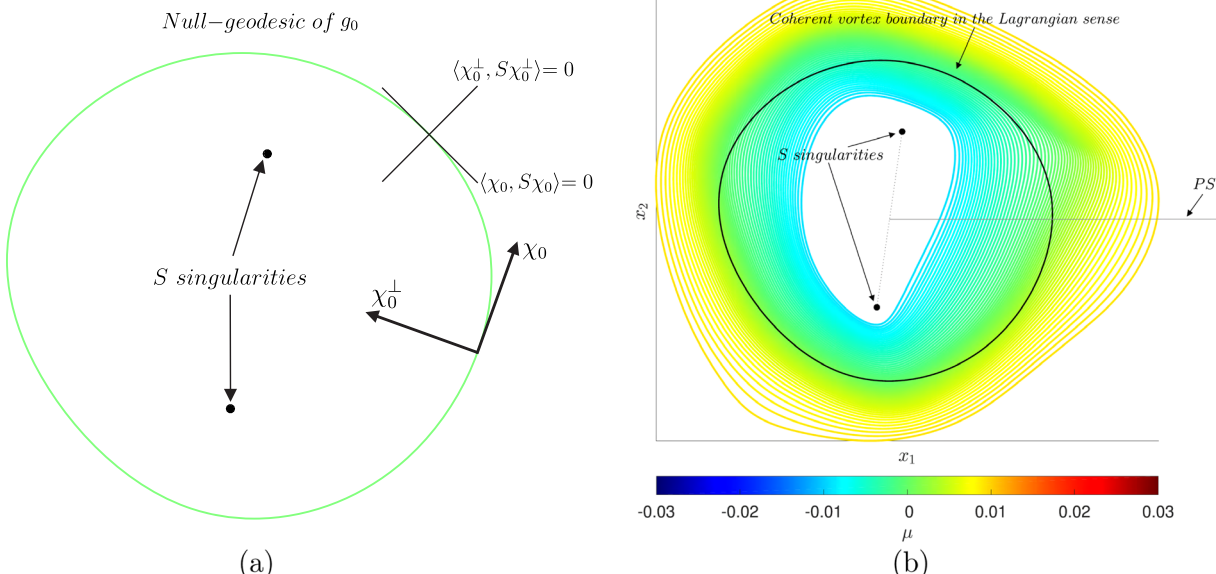


FIG. 3. (a) Perfectly coherent elliptic OECS at time  $t$ , obtained as a limit cycle  $\gamma$  of the direction field  $\chi_\mu^\pm(x, t)$ . The tangential stretching rate (and, in incompressible flows, the normal repulsion rate) along  $\gamma$  is pointwise zero. Furthermore, the interior of  $\gamma$  always contains at least two singularities of the tensor field  $S$ . (b) Nested family of elliptic OECSs for different values of  $\mu$  (in color). A nearby Lagrangian vortex boundary is shown in black. Black dots represent singularities of the rate-of-strain tensor used for an automatic placement of the Poincaré Section (PS) in the detection of limit cycles for the direction field family  $\chi_\mu^\pm(x, t)$ .

(BC1) *Variable-endpoint boundary conditions*: The endpoints of  $\gamma$  coincide with singularities of the rate-of-strain tensor field  $S(x, t)$ , i.e., we have  $s_1(x(0), t) = s_2(x(0), t)$  and  $s_1(x(\sigma), t) = s_2(x(\sigma), t)$ . In this case, the perturbations  $h(s)$  are arbitrary, including arbitrary perturbations to the endpoints of  $\gamma$ .

(BC2) *Fixed-endpoint boundary conditions*: The perturbation  $h(s)$  is arbitrary for all  $s \in (0, \sigma)$ , but must leave the endpoints of  $\gamma$  fixed:  $h(0) = h(\sigma) = 0$ .

Under (BC1) or (BC2), the bracketed term in (14) vanishes. By the fundamental lemma of the calculus of variations, a solution curve  $\gamma$  of (14) must then satisfy the Euler–Lagrange equations

$$\partial_x \dot{p} - \frac{d}{ds} \partial_{x'} \dot{p} = 0. \quad (18)$$

Invoking the results of Ref. 10 for shearless LCSs, we obtain that solution curves of (18) with exactly vanishing shear rates are piecewise tangent to one of the eigenvector fields of  $S(x, t)$ .

**Theorem 2.** *Shearless OECSSs at time  $t$  coincide with continuous trajectories of the differential equation family*

$$\frac{dx}{ds} = e_i(x, t), \quad S(x, t)e_i(x, t) = s_i(x, t)e_i(x, t), \quad i = 1, 2. \quad (19)$$

Along any such shearless OECSS, the pointwise material shear rate at time  $t$  is zero.

We refer to the trajectories of (19) as  $e_1$ -lines and  $e_2$ -lines, respectively. We will use the boundary condition classes (BC1) and (BC2) to further distinguish parabolic and hyperbolic OECSSs within the shearless OECSSs satisfying (19).

From an argument closely following,<sup>10</sup> we obtain that the solutions of (18) can also be viewed as null-geodesics of the Lorentzian metric family

$$m_\nu(u, u) = \langle u, [2S(x, t)R - \nu I]u \rangle, \quad \nu \in \mathbb{R},$$

which again has metric signature  $(-, +)$ ,<sup>2</sup> and admits singularities at locations of repeated eigenvalues of  $S(x, t)$ . In particular, shearless OECSSs are null geodesics of  $m_\nu(u, u)$  for  $\nu = 0$ .

## A. Parabolic OECSS

*Parabolic OECSSs* are trajectories of (19) that satisfy the free-endpoint boundary conditions (BC1) and are as close as possible to being neutrally stable, as detailed below. By the nature of (BC1), such OECSSs are stationary curves of the shear-rate functional  $\dot{P}_t(\gamma)$  under the broadest possible set of perturbations. This makes parabolic OECSSs the most observable class of shearless OECSSs, creating *short-term pathways* that mimic the role of the Lagrangian jet cores identified in Ref. 10. The higher robustness of parabolic OECSSs implies a more pronounced signature in tracer patterns. This is consistent with observations of tracers and scalar fields that highlight the details of jet cores more prominently than those of hyperbolic structures.

Parabolic OECSSs are heteroclinic chains of  $e_1$ -lines and  $e_2$ -lines connecting singularities of  $S(x, t)$ . For observability and uniqueness, we only consider alternating chains of  $e_1$ - and  $e_2$ -line connections that are locally unique and structurally stable. As shown in Ref. 8, the only structurally stable tensorline singularities are trisectors and wedges, shown in Fig. 4.

Furthermore, as shown in Ref. 10, a structurally stable and unique connection between two such singularities must necessarily be a wedge-trisector connection, as illustrated in Fig. 5. By definition, each segment of an alternating chain of  $e_1$ - and  $e_2$ -lines repels or attracts trajectories over short enough time intervals. To ensure that neither attraction nor repulsion prevails for the whole trajectory chain, we require the chain to be as close as possible to being neutrally stable. To this end, we introduce the pointwise *neutrality functions*

$$\mathcal{N}_{e_1}(x, t) = s_2^2(x, t), \quad \mathcal{N}_{e_2}(x, t) = s_1^2(x, t), \quad (20)$$

with the function  $\mathcal{N}_{e_i}(x, t)$  measuring how close the squared rate of attraction or repulsion,  $s_j^2(x, t)$ , along an  $e_i$  line is to zero at time  $t$ . In case of incompressible flows, we have  $\mathcal{N}_{e_1}(x, t) = \mathcal{N}_{e_2}(x, t)$ , given that  $s_1(x, t) + s_2(x, t) = 0$ .

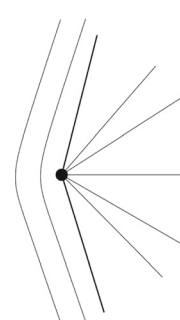
All this follows closely the variational approach developed in Ref. 10 for parabolic LCSs, but with  $S(x, t)$  substituted for  $C_{t_0}^t(x_0)$ . As a next step, we introduce the convexity sets

$$\begin{aligned} \mathcal{C}_{e_i}(t) = \{x \in U : \langle e_j(x, t), \partial_r^2 \mathcal{N}_{e_i}(x, t) e_j(x, t) \rangle > 0, i \neq j\}, \\ i = 1, 2. \end{aligned} \quad (21)$$

Each such set  $\mathcal{C}_{e_i}(t)$  is simply the set of points at which the corresponding neutrality  $\mathcal{N}_{e_i}(x, t)$  is a convex function of  $x$  at time  $t$ . We say that a compact  $e_i$ -line segment  $\gamma$  is a *weak minimizer* of  $\mathcal{N}_{e_i}$  at time  $t$  if both  $\gamma$  and the nearest trench of the function  $\mathcal{N}_{e_i}(\cdot, t)$  lie in the same connected component of  $\mathcal{C}_{e_i}(t)$ . More precisely, if the arclength parametrization of  $\gamma$  is  $x(s)$ , and the unit normal along  $\gamma$  is given by  $n(s)$ , then we require

$$x(s) + \epsilon n(s) \in \mathcal{C}_{e_i}(t), \quad s \in [0, \sigma], \quad \epsilon \in [0, \epsilon_0(s, t)], \quad (22)$$

Wedge



Trisector

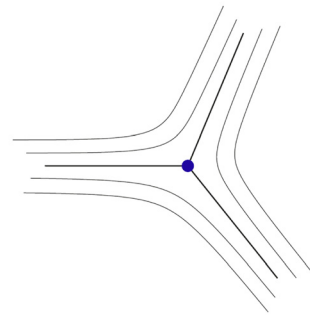


FIG. 4. Local topology of a tensorline field around structurally stable singularities: Wedge and Trisector.

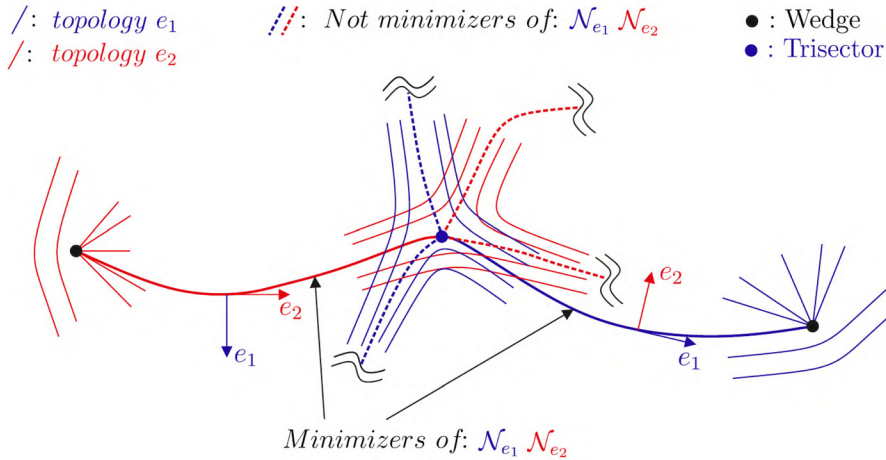


FIG. 5. Parabolic OECSSs are alternating chains of  $e_i$ -lines that connect structurally stable singularities and are weak minimizers of the corresponding neutrality functions  $\mathcal{N}_{e_i}$ .

where

$$\epsilon_0(s, t) = \min\{|\epsilon| \in \mathbb{R}^+ : \partial_\epsilon \mathcal{N}_{e_i}(x(s) + \epsilon n(s), t) = 0, \partial_\epsilon^2 \mathcal{N}_{e_i}(x(s) + \epsilon n(s), t) > 0\}. \quad (23)$$

We summarize our formal definition of parabolic OECSSs as follows (cf. Fig. 5).

**Definition 4.** A *parabolic OECSS* at time  $t$  is a shearless OECSS composed of alternating chains of  $e_1$ - and  $e_2$ -line segments that connect wedge and trisector singularities of the rate-of-strain tensor  $S(x, t)$ . Furthermore, each  $e_i$  segment in the chain is a weak minimizer of the neutrality function  $\mathcal{N}_{e_i}(x, t)$ .

## B. Hyperbolic OECSSs

*Hyperbolic OECSSs* are trajectory segments of (19) that satisfy the fixed-endpoint boundary conditions (BC2) and contain precisely one point of maximal repulsion-rate or maximal attraction-rate. This point will then play the role of

an instantaneous saddle point, with the OECSSs acting as the short-term stable or unstable manifold for this saddle point. By the nature of (BC2), hyperbolic OECSSs are only stationary curves of the shear-rate functional  $\dot{P}_t(\gamma)$  under variations that leave their endpoints fixed. This makes individual hyperbolic OECSSs less observable than the parabolic OECSSs. This is also the case for hyperbolic LCSs, which are generally responsible for the intricate filamentation of tracer patterns. Details of these filaments are generally less observable and robust as those of Lagrangian jet cores marked by parabolic LCSs (cf. Ref. 10).

Within the family of hyperbolic OECSSs, we distinguish *attracting OECSSs* as material curves that attract nearby material curves instantaneously. Similarly, we distinguish *repelling OECSSs* as hyperbolic OECSSs that instantaneously repel all nearby material curves. We summarize these definitions more formally as follows (cf. Fig. 6).

**Definition 5.** A *repelling OECSS* at time  $t$  is an open  $e_1$ -line segment that contains a local maximum of the function  $s_2(\cdot, t)$ , but contains no other local extremum point of  $s_2(\cdot, t)$ . An *attracting OECSS* at time  $t$  is an open  $e_2$ -line

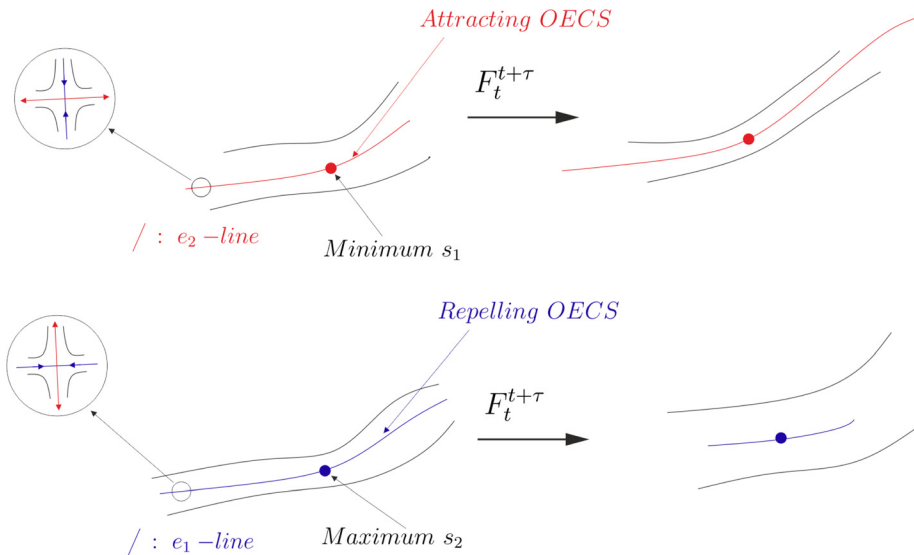


FIG. 6. Attracting (repelling) hyperbolic OECSSs as the instantaneous attracting (repelling) material lines launched from a minimum of  $s_1$  (maximum of  $s_2$ ). In the circular inset: the local tangential stretching and normal repulsion.

segment that contains a local minimum of the function  $s_1(\cdot, t)$ , but contains no other local extremum of  $s_1(\cdot, t)$ . Finally, a *hyperbolic O ECS* is a shearless O ECS that is either an attracting or a repelling O ECS.

*Remark 1.* As indicated in Fig. 6, the cores of hyperbolic O ECSSs are defined by a local maximum of  $s_2(\cdot, t)$  along repelling O ECSSs and by a local minimum of  $s_1(\cdot, t)$  along attracting O ECSSs. We call these cores *objective saddle points*, as they represent generalizations of classic saddle-type stagnation points from steady flows. Close to objective saddle points, hyperbolic O ECSSs induce the strongest saddle-type deformation on nearby particles along the directions shown in the circular insets of Fig. 6. Instantaneous stagnation points of an unsteady velocity field are not Galilean invariant, i.e., may disappear even under constant-speed translations of the coordinate frame (cf. Fig. 1). In contrast, the objective saddle points introduced here are objective, and hence persist even under general observer changes of form (1). The local value of  $s_i(x, t)$  on the objective saddle quantifies the strength of that saddle objectively.

## VII. SUMMARY OF OECSSS AND THEIR NUMERICAL IDENTIFICATION

In Table I, we list the OECSSs we introduced in Sec. V–VI, together with the ODEs and boundary conditions they satisfy.

Next, we summarize the numerical steps in locating OECSSs in a planar unsteady flow. We start with the common steps, then detail the further steps for different types of OECSSs separately.

---

**Algorithm 1.** Compute the rate-of-strain tensor  $S(x, t)$ , its invariants and singularities.

---

**Input:** A two-dimensional velocity field  $v(x, t)$

1. Compute the rate-of-strain tensor  $S(x, t) = \frac{1}{2} \left( \nabla v(x, t) + [\nabla v(x, t)]^T \right)$  at the current time  $t$  on a rectangular grid over the  $(x_1, x_2)$  coordinates.
2. Detect the singularities of  $S$  as common, transverse zeros of  $S_{11}(\cdot, t) - S_{22}(\cdot, t)$  and  $S_{12}(\cdot, t)$ , with  $S_{ij}$  denoting the entry of  $S$  at row  $i$  and column  $j$ .
3. Determine the type of the singularity (trisector or wedge) as described in Ref. 10.
4. Compute the eigenvalue fields  $s_1(x, t) < s_2(x, t)$  and the associated unit eigenvector fields  $e_i(x, t)$  of  $S(x, t)$  for  $i = 1, 2$ .

**Output:**  $S(x, t)$  as well as  $s_i(x, t)$  and  $e_i(x, t)$ , for  $i = 1, 2$ , and the position and type (wedge or trisector) of the rate-of-strain singularities  $x^j(t)$  satisfying  $s_1(x^j(t), t) = s_2(x^j(t), t)$ ,  $j = 1, \dots, N$ .

---

## A. Elliptic OECSSs

To locate elliptic OECSSs automatically as limit cycles of the direction field (16), we rely on a version of Poincaré's

TABLE I. Summary of the different types of OECSSs.

Type of OECSS	ODE	Boundary conditions
Attracting	$x' = e_2(x, t)$	Arbitrary; $x(s)$ contains a local minimum of $s_1(\cdot, t)$
Repelling	$x' = e_1(x, t)$	Arbitrary; $x(s)$ contains a local maximum of $s_2(\cdot, t)$
Parabolic	$x' = e_i(x, t)$ with alternating $i$	$s_2(x, t) = s_1(x, t)$
Elliptic	$x' = \chi_\mu^\pm(x, t)$	Periodic

index theory extended to direction fields.<sup>7,22</sup> A consequence of this theory is that at least two wedge-type singularities of  $S(x, t)$  must exist inside any such limit cycle.<sup>22</sup> For robust limit cycles, we seek nearby wedge pairs surrounded by an annular region of no singularities. The same procedure arises in an elliptic LCS detection, involving the location of singularities of the tensor field  $C_{t_0}^{t_1}$ . We refer to Ref. 22 for details of this numerical algorithm.

---

**Algorithm 2.** Compute Elliptic OECSSs.

---

**Input:**  $S(x, t)$  as well as  $s_i(x, t)$  and  $e_i(x, t)$ , for  $i = 1, 2$ , and the position and type (wedge or trisector) of the rate-of-strain singularities  $x^j(t)$  satisfying  $s_1(x^j(t), t) = s_2(x^j(t), t)$ ,  $j = 1, \dots, N$ .

1. Locate isolated wedge-type pairs of singularities and place the Poincaré sections at their midpoint.
2. Compute the vector field  $\chi_\mu^\pm(x(s), t)$  defined in (16) for different values of stretching rate  $\mu$ , remaining in the range  $\mu \approx 0$ .
3. Use the Poincaré sections as sets of initial conditions in the computation of limit cycles of

$$x'(s) = \text{sign} \left\langle \chi_\mu^\pm(x(s)), \frac{dx(s - \Delta)}{ds} \right\rangle \chi_\mu^\pm(x(s)),$$

where the factor multiplying  $\chi_\mu^\pm(x(s), t)$  removes potential orientational discontinuities in the direction field  $\chi_\mu^\pm(x(s), t)$  away from singularities, and  $\Delta$  denotes the integration step in the independent variable  $s$ .

**Output:** Elliptic OECSSs.

---

## B. Hyperbolic OECSSs

---

**Algorithm 3.** Compute Hyperbolic OECSSs.

---

**Input:**  $S(x, t)$  as well as  $s_i(x, t)$  and  $e_i(x, t)$ , for  $i = 1, 2$ .

1. Compute the sets  $\mathcal{S}_{im}(t)$  of isolated local maxima of  $|s_i(\cdot, t)|$  for  $i = 1, 2$ .
2. Compute attracting OECSSs ( $e_2$ -lines) as solutions of the ODE

$$\begin{cases} x'(s) = \text{sign} \left\langle e_2(x(s)), \frac{dx(s - \Delta)}{ds} \right\rangle e_2(x(s)) \\ x(0) \in \mathcal{S}_{1m}. \end{cases}$$

Stop integration when  $|s_1(x(s))|$  ceases to be monotone decreasing.

3. Compute repelling OECSSs ( $e_1$ -lines) as solutions of the ODE

$$\begin{cases} x'(s) = \text{sign} \left\langle e_1(x(s)), \frac{dx(s - \Delta)}{ds} \right\rangle e_1(x(s)) \\ x(0) \in \mathcal{S}_{2m}. \end{cases}$$

Stop integration when  $|s_2(x(s))|$  ceases to be monotone decreasing.

**Output:** Hyperbolic OECSSs.

---

### C. Parabolic OECSSs

**Algorithm 4.** Compute Parabolic OECSSs.

**Input:**  $S(x, t)$  as well as  $s_i(x, t)$  and  $e_i(x, t)$ , for  $i = 1, 2$ , and the position and type (wedge or trisector) of the rate-of-strain singularities  $x^j(t)$  satisfying  $s_1(x^j(t), t) = s_2(x^j(t), t)$ ,  $j = 1, \dots, N$ .

1. For each trisector-type singularity  $x^j(t)$ , compute the  $e_1$ -lines and  $e_2$ -lines connecting the trisector to a wedge.
2. Out of these heteroclinic connections, keep only those that are weak minimizers of the corresponding neutrality function  $\mathcal{N}_{e_i}$ ,  $i = 1, 2$  (cf. Equations (20)–(23).)
3. With the separatrices obtained in this fashion, build alternating chains of heteroclinic  $e_1$ -lines and  $e_2$ -lines

**Output:** Parabolic OECSSs.

## VIII. EXAMPLE: MESOSCALE OECSSs IN LARGE-SCALE OCEAN DATA

We use Algorithms 1–4 from Section VII to locate OECSSs in a two-dimensional ocean surface velocity data set derived from AVISO satellite altimetry measurements (<http://www.aviso.oceanobs.com>). The domain of interest is the Agulhas leakage in the Southern Ocean bounded by longitudes [17°W, 7°E], latitudes [38°S, 22°S], and the time slice we selected correspond to  $t = 24$  November 2006.

Under the geostrophic assumptions, the ocean surface height measured by satellites plays the role of a streamfunction for surface currents. With  $h$  denoting the sea surface height, the velocity field in longitude latitude coordinates,  $[\phi, \theta]$ , can be expressed as

$$\begin{aligned}\dot{\phi} &= -\frac{g}{R^2 f(\theta) \cos \theta} \partial_\theta h(\phi, \theta, t), \\ \dot{\theta} &= \frac{g}{R^2 f(\theta) \cos \theta} \partial_\phi h(\phi, \theta, t),\end{aligned}$$

where  $f(\theta) := 2\Omega \sin \theta$  denotes the Coriolis parameter,  $g$  is the constant of gravity,  $R$  is the mean radius of the earth and  $\Omega$  its mean angular velocity. The velocity field is available at weekly intervals, with a spatial longitude-latitude resolution of  $0.25^\circ$ . For more details on the data, see Ref. 3.

### A. Elliptic OECSSs

Following Algorithm 1 in Section VII A, we locate singularities of the rate-of-strain tensor  $S(x, t)$ , and discard isolated wedge singularities whose distance to the closest wedge point is larger than the typical mesoscale distance of  $2^\circ \approx 200$  km. The remaining wedge pairs mark candidate regions for elliptic OECSSs.

Along with elliptic OECSSs, we will also show the value of the Okubo–Weiss (OW) parameter

$$OW(x, t) = s_2^2(x, t) - \omega^2(x, t),$$

where  $\omega(x, t)$  denotes the vorticity. Spatial domains with  $OW(x, t) < 0$  are frequently used indicator of an instantaneous ellipticity in the unsteady fluid flows.<sup>27,33</sup> While the OW

parameter is not objective (the vorticity term will change under rotations), its simplicity makes it broadly used in locating coherent vortices.

In the domain of study, we obtain a total of eighteen objectively detected vortical regions, each filled with families of elliptic OECSSs. We plot these families over a two-dimensional graph of  $-OW(x, t)$ , and also project them onto the level curves of  $-OW(x, t)$  in the plane (Fig. 7).

Note that the objective vortical regions E#18, E#8 and E#2 arise in regions where  $-OW(x, t)$  is nearly zero and hence indicates no significant vortical activity. At the same time, at the bottom right region of the domain,  $OW(x, t)$  attains several strong local minima, even though there are no elliptic OECSSs present (cf. Fig. 7(b)). As a representative example, we show in Fig. 8 the three strongest local minima of  $OW(x, t)$  in this region along with the deformation of material blobs, initially centered on those minima, for an integration time of six days. For comparison, Fig. 9 shows the deformation experienced by blobs initialized within two elliptic OECSSs (E#11, E#13) for different integration times, up to six days.

The blobs in Fig. 9 barely deform, and hence instantaneously computed elliptic OECSSs exhibit short-term Lagrangian vortex-type behavior, as expected.

Hence, the regions of highest ellipticity for the Okubo–Weiss parameter show significant stretching, while regions identified by elliptic OECSSs remain highly coherent over the same time interval. We have, therefore, clear examples of both false positives and false negatives for Okubo–Weiss-based vortex detection.

The vortical regions #2, #6, #8, #11, #13, #15, #18 approximate locations where exceptionally coherent Lagrangian coherent eddies have been found in other studies (see Refs. 22 and 18). These Lagrangian studies cover a time interval of three months, with their initial time coinciding with the time of the present Eulerian analysis. Remarkably, about one third of the elliptic OECSSs we find are signatures of elliptic LCSs with long-term coherence.

Figure 10 underlines this observation by showing the top view of Fig. 7(a) separately, using a different colormap for the  $-OW(x, t)$  scalar field, and tagging with red numbers elliptic OECSSs in the coherent Lagrangian eddy domains identified in Ref. 18. Without exception, these regions are marked by near-zero values of the stretching rate, indicating a high degree of Eulerian coherence for the elliptic OECSSs. A rigorous treatment of short-term Lagrangian forecasting based on the OECSSs will appear elsewhere. In the absence of such a treatment, the time scales over which the OECSS-based predictions are valid are problem-dependent.

In contrast, most of these highly coherent Lagrangian eddies have very moderate signatures in the contour plot of the Okubo–Weiss parameter. Taking all regions of closed  $OW(x, t)$  level sets with comparable values as predictions for coherent eddies would result in an order-of-magnitude over-prediction for vortical regions. This is consistent with the findings of Ref. 3, which reports a roughly tenfold over-prediction of the actual number of coherent Agulhas eddies by the Okubo–Weiss criterion.

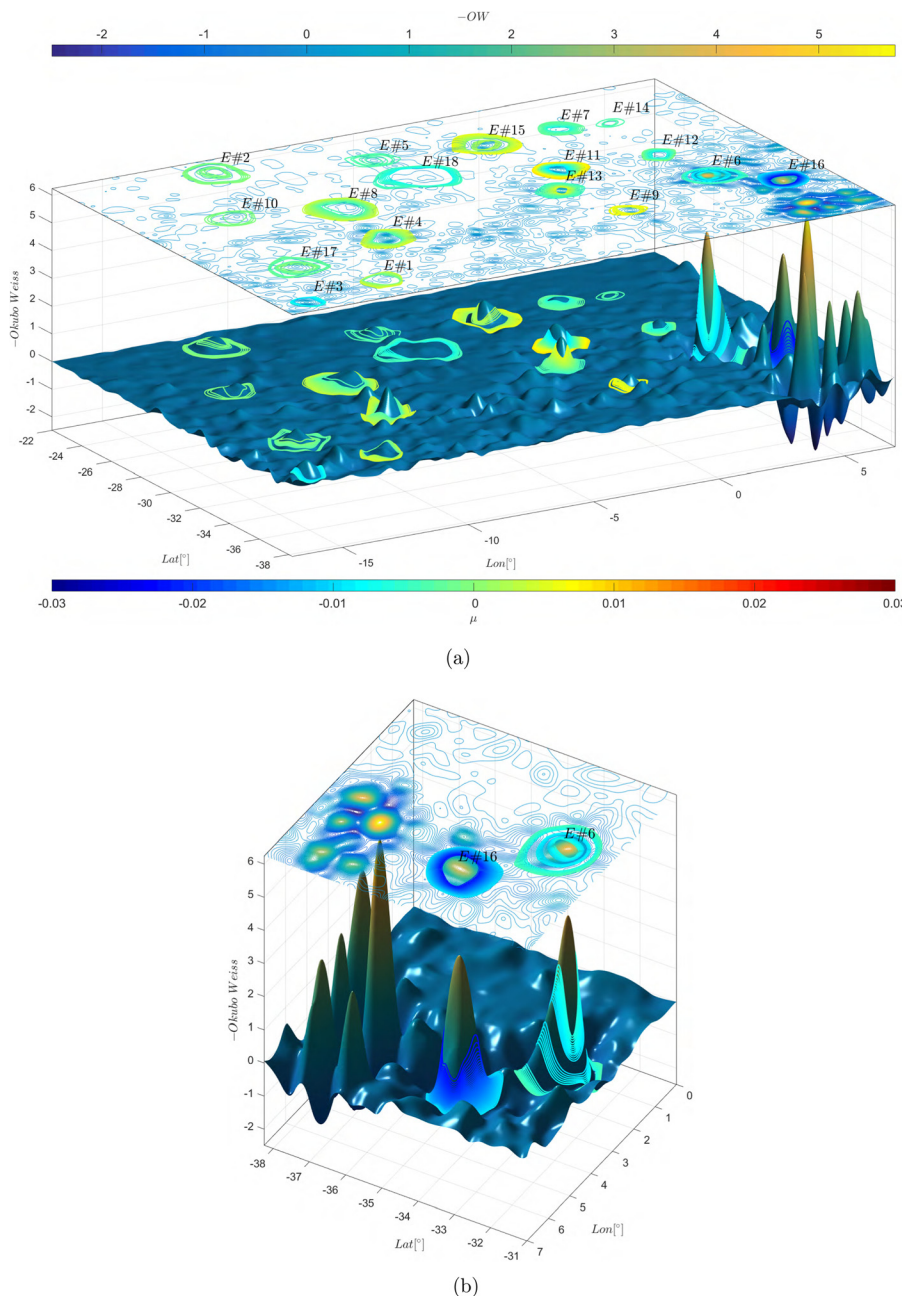


FIG. 7. (a) Elliptic OECs for different values of stretching rate  $\mu$  (bottom colorbar) on a surface representing the magnitude of  $-OW(x, t)$  (upper colorbar or z-axis). On top, the same elliptic OECs are shown over level sets of  $-OW$ . Black numbers label vortical regions foliated by families of elliptic OECs. (b) A different view for the bottom-right part of the same domain.

## B. Hyperbolic OECs

We compute hyperbolic OECs at the same time used in our elliptic OECs calculations, on a subdomain bounded by longitudes [2.5°E, 7°E] and latitudes [38.25°S, 36°S]. Since the velocity field is incompressible ( $Tr(S) = s_1 + s_2 = 0$ ), the maxima of  $s_2$  coincide with the minima of  $s_1$ . Consequently, the same OECs cores arise as starting points in the computation of both attracting and repelling hyperbolic OECs. We show all hyperbolic OECs as obtained in Fig. 11. As noted earlier, the cores of hyperbolic OECs represent the *objective saddle points* in the unsteady velocity field. In a general compressible flow, the cores of attracting and repelling hyperbolic OECs are distinct, and the corresponding OECs, generally, do not intersect each other.

Figure 11 (Multimedia view) shows how hyperbolic OECs act as instantaneous stable and unstable manifolds for

short-term particle motion. Remarkably, several hyperbolic OECs cross the local streamlines at large angles at the initial time (Fig. 11(a)), as well as at later times (Figs. 11(b)–11(d)), explaining the deformation of nearby blobs of fluid. In particular, the *objective saddle point* (cf. Remark 1) captured by a hyperbolic OEC (point A in Figs. 11(a) and 11(d)) induces markedly hyperbolic short-term Lagrangian behavior even though it is located within an area of closed streamlines. In a similarly surprising fashion, the *objective saddle points* B and C create significant short-term material stretching in a direction perpendicular to the local streamlines. Black numbers label objective saddles in decreasing strength (i.e., decreasing  $s_2$  values). Figure 11(d) shows that this order correlates strongly with the actual material deformation induced on nearby sets of particles.

Figure 12 presents the same results as Fig. 11(d) but over level sets of the negative Okubo–Weiss parameter

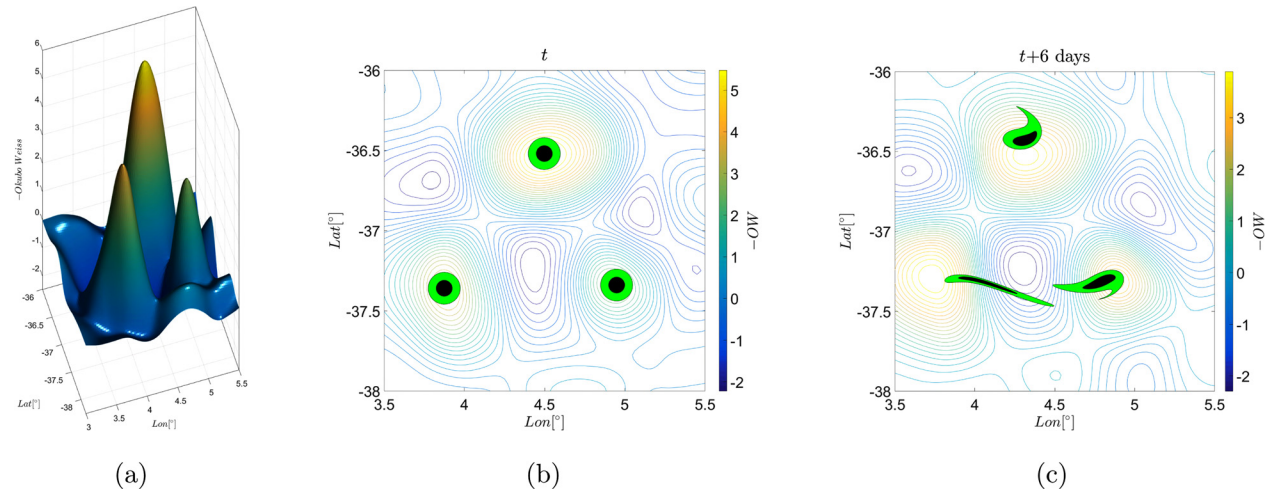


FIG. 8. (a) Strongest local minima of  $OW(x, t)$  in the bottom right region of the domain. (b) Material blobs of initial conditions centered on local minima of  $OW(x, t)$ . (c) Deformed material blobs after six days.

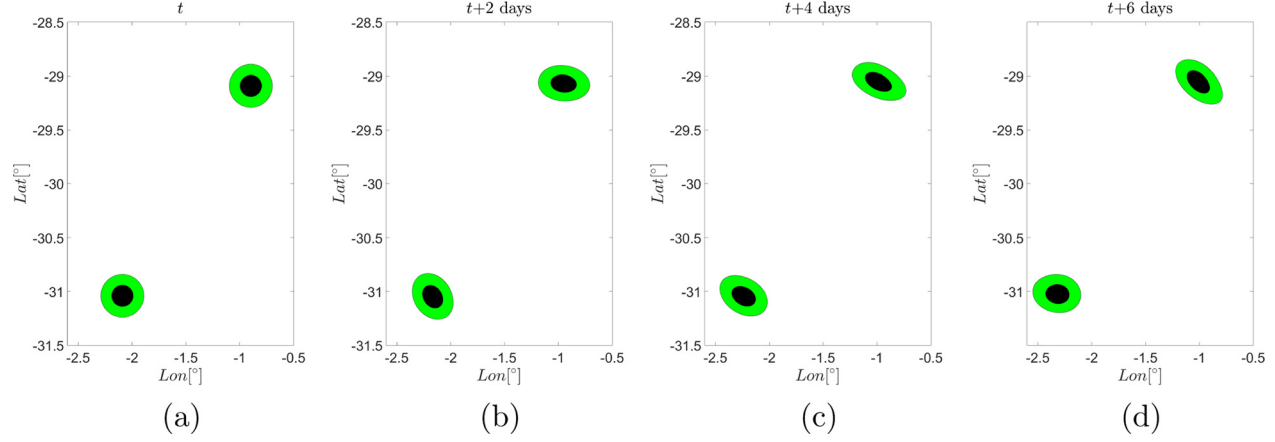


FIG. 9. Moderate deformation experienced by material blobs of initial conditions released within the elliptic OECSSs  $E\#11$  and  $E\#13$ .

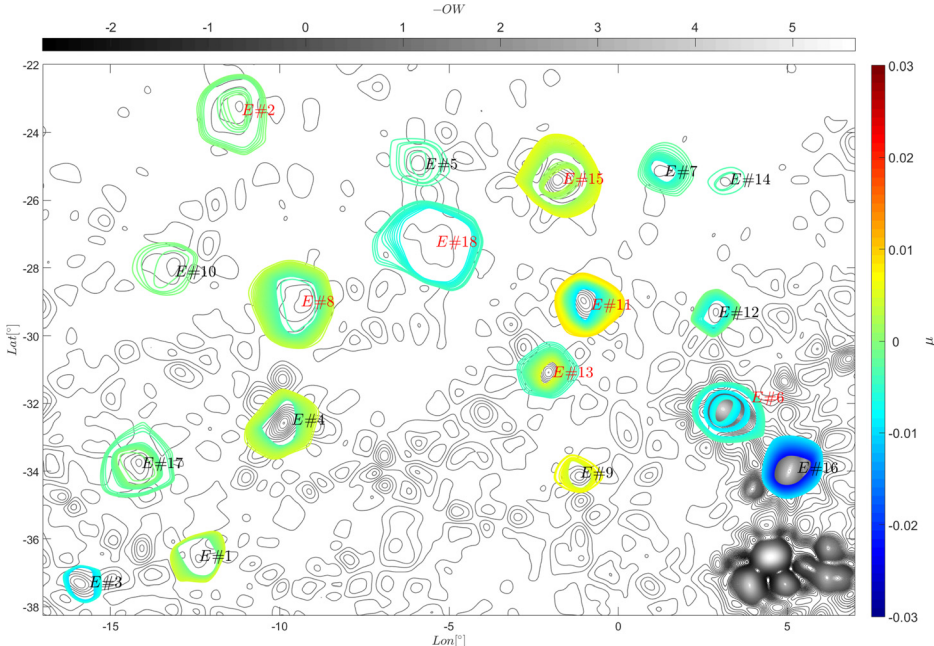


FIG. 10. Top view of Fig. 7(a) with a different colormap for the negative  $OW(x, t)$  parameter. Red numbers identify elliptic OECSSs located in regions where exceptionally coherent Lagrangian eddies have been found.

$-OW(x, t)$ . Note how some hyperbolic OECSSs cross closed contours around local minima of  $OW(x, t)$  that are generally believed to signal elliptic regions.

Figure 13 illustrates that attracting OECSSs continues to shape the short-term tracer deformation patterns in larger distances from their cores, for times up to six days. Over this time interval, material blobs align with materially advected  $e_2$ -lines, underlining the role of attracting OECSSs as short-term unstable manifolds.

A common Eulerian diagnostic for short-term hyperbolic tracer behavior is the identification of instantaneous saddle-type stagnation points in the velocity field. For comparison with this diagnostic, we show in Fig. 14(a) the only three saddle-type stagnation points (magenta triangles) that exist instantaneously in the domain at time  $t = 24$  November 2006. Also shown are the corresponding stable (dashed blue lines) and unstable (dashed red lines) directions inferred from streamlines (black lines) for these stagnation points, along with the ten *objective saddle points* (red dots) found at the same time instant.

Two of these red dots marking hyperbolic OECSS cores in Fig. 14 fall near two instantaneous stagnation points, and give an improved objective prediction for the cores of short-term saddle-type behavior in Lagrangian particle motion. The improvement is seen by tracking the deformation of the advected fluid blobs, initially centered on the stagnation

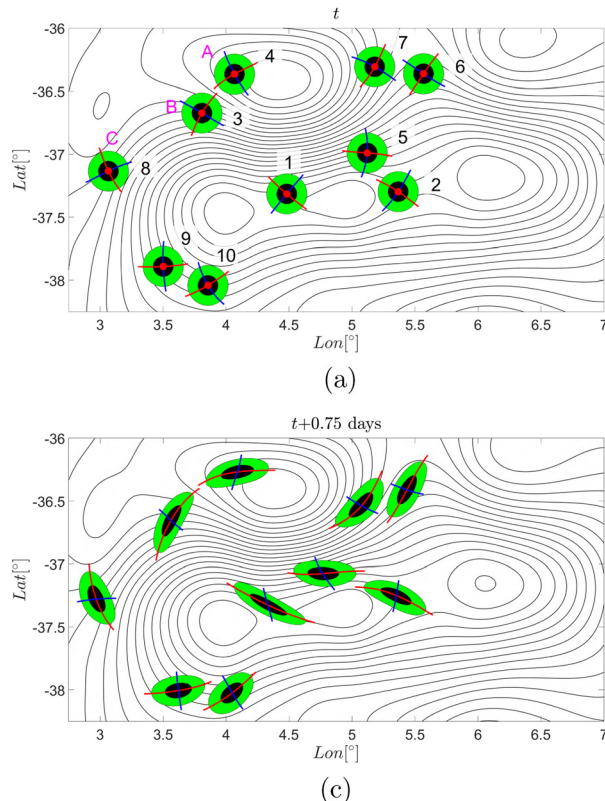


FIG. 11. (a) Hyperbolic OECSSs: attracting (red) and repelling (blue) overlaid on streamlines. The red dots denote the *objective saddle points* (cores of the OECSSs), i.e., maxima of  $s_2$ , which coincide with the minima of  $s_1$  in the present incompressible flow. (b)–(d) Advected images of the hyperbolic OECSSs up to 1.5 days and their effect on nearby particles. Black numbers label hyperbolic OECSSs in decreasing order of  $s_2$ . Magenta letters identify hyperbolic OECSSs inducing short-term Lagrangian stretching completely hidden in the streamline geometry. A: Observed hyperbolic behavior within closed instantaneous streamlines. B and C: Hyperbolic OECSSs showing significant stretching, with attracting OECSSs perpendicular to the streamlines. (Multimedia view) [URL: <http://dx.doi.org/10.1063/1.4951720.1>]

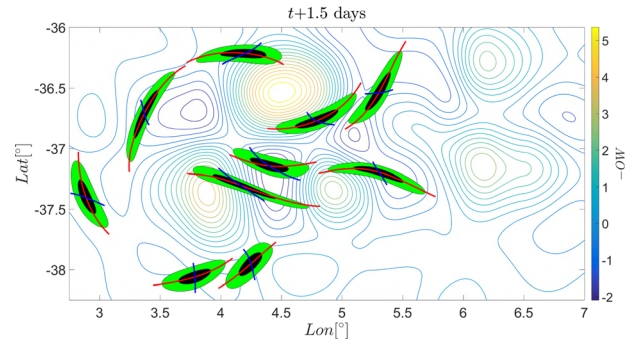
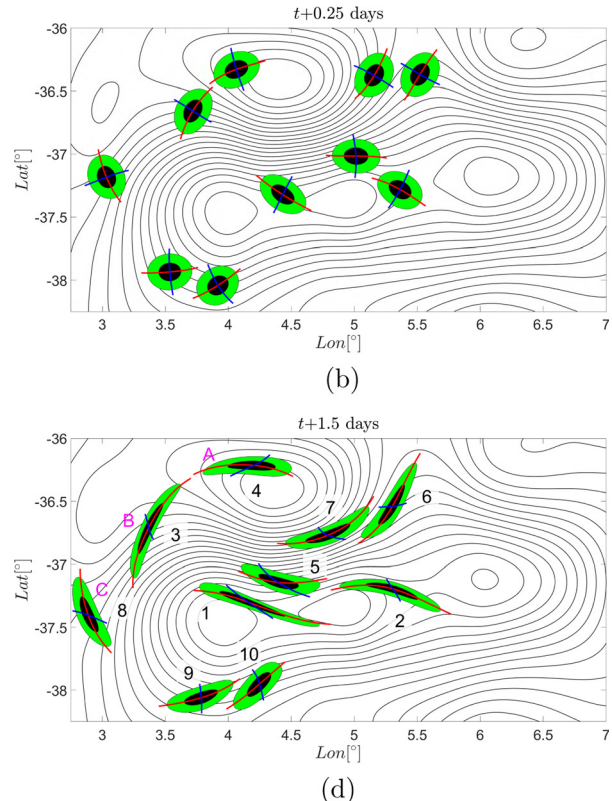


FIG. 12. (a) Same figure as Fig. 11(d) with level sets of  $-OW(x, t)$  in the background.

points. These blobs must stretch as they lie close to two *objective saddle points*. The stretching blobs, however, align more closely with the advected  $e_2$ -lines shown in Fig. 11 when compared to the advected streamline segments shown in Fig. 14. The instantaneous stagnation point on the top left, instead, induces no notable material stretching on nearby particles since there are no hyperbolic OECSS cores in its vicinity. The remaining eight hyperbolic OECSSs remain completely hidden in the instantaneous streamline picture (cf. Fig. 14), even though they induce significant saddle-type material stretching, as we have already seen in Fig. 11.



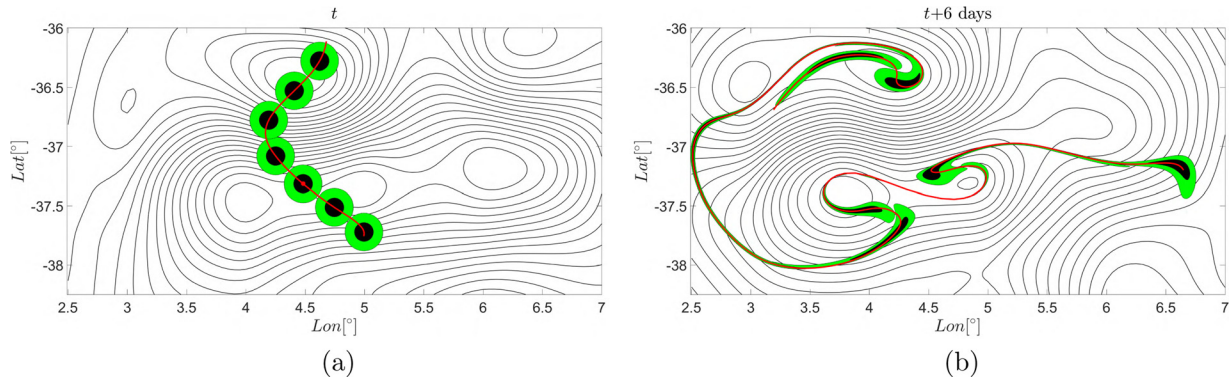


FIG. 13. (a) More extended view of an attracting OECS, with blobs of initial conditions placed along the OECS, overlaid on streamlines. (b) Adverted image of the OECS and of the marked initial conditions for 6 days.

These results illustrate that an instantaneous forecast strategy based on the saddle-type stagnation points of the velocity field may miss the majority of significant short-term material stretching events in the flow. Even for the detected stagnation points, there is no guarantee that they signal nearby Lagrangian hyperbolic behavior correctly, unless the velocity field has slow enough variation in their vicinity.<sup>20</sup> This mismatch between objective and frame-dependent predictions for saddle points is generally expected to increase further for highly unsteady flows.

### C. Parabolic OECSs

We now discuss the existence of parabolic OECSs in the full domain used for computing elliptic OECSs. There is no known persistent Eulerian or Lagrangian jet in this part of the ocean, but we nevertheless uncover parabolic OECSs in this region that act as short-term pathways for material transport.

In Fig. 15, we show three parabolic OECSs obtained from the application of Algorithm 4 to the velocity data studied here. These OECSs are, therefore, alternating chains of

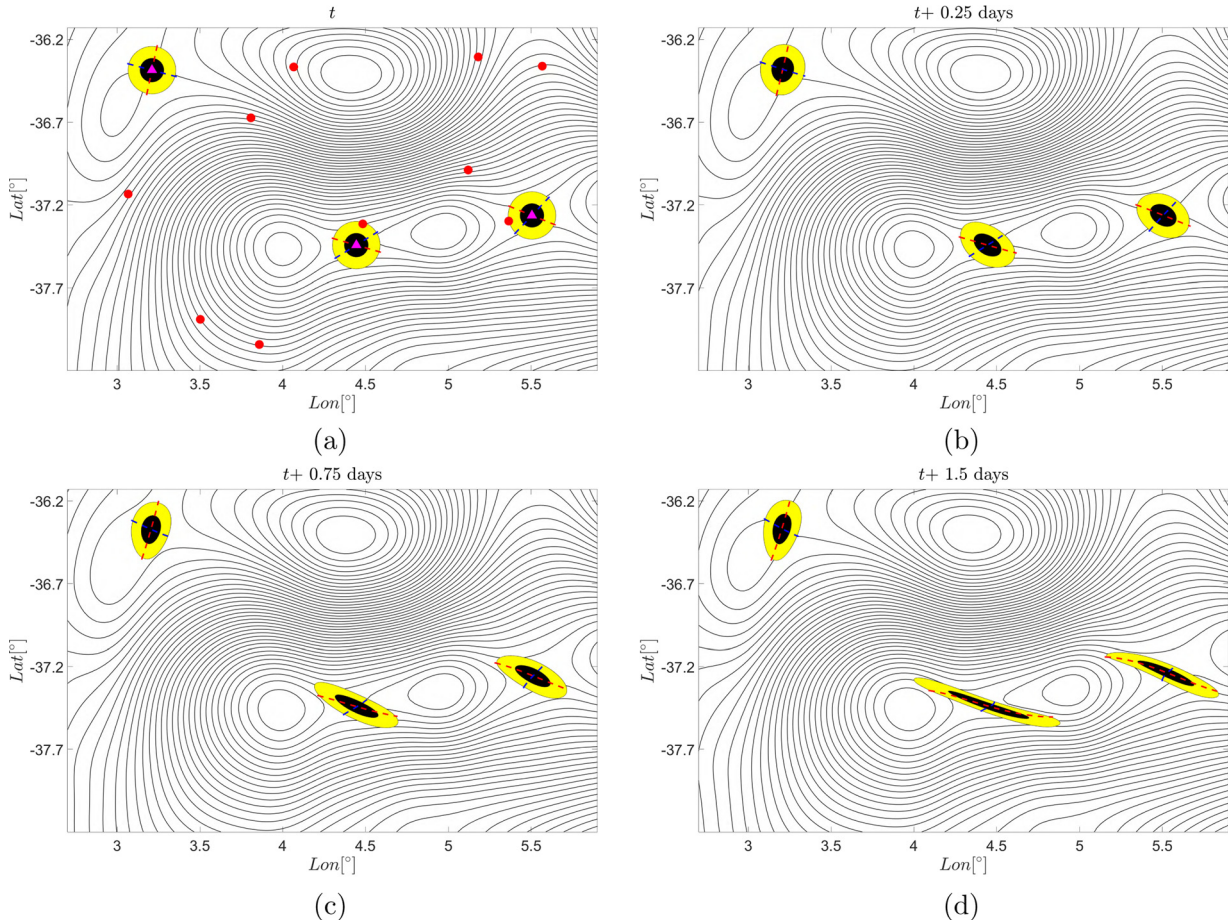


FIG. 14. (a) Saddle-type stagnation points of the velocity field (magenta triangles) with their associated stable (dashed blue lines) and unstable (dashed red lines) streamlines. Red dots denote the objective saddle points at the same time instant. (b)–(d) Adverted images of the stable and unstable streamlines of saddle-type stagnation points up to 1.5 days and their effects on nearby particles.

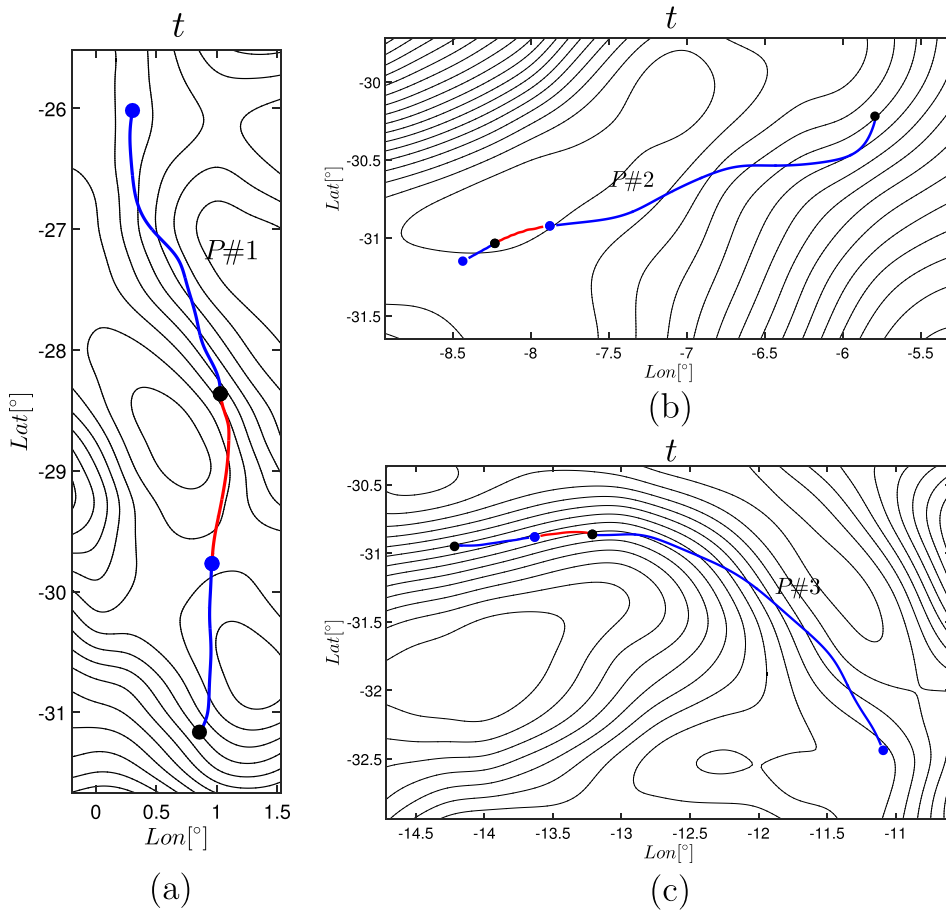


FIG. 15. (a)–(c) Parabolic OECSSs as alternating heteroclinic connections of  $e_1$ -lines (blue) and  $e_2$ -lines (red) between trisector-type singularities (blue dots) and wedge-type singularities (black dots). Instantaneous streamlines are shown in the background.

$e_1$ -lines (blue) and  $e_2$ -lines (red), connecting trisector-type (blue dots) singularities and wedge-type singularities (black dots), with the streamlines shown in the background for reference. The three parabolic OECSSs are of approximate sizes 500 km for P#1 and 300 km for P#2 and P#3.

As a representative example, Fig. 16 (Multimedia view) shows the advected positions of the parabolic OECSS, P#3, along with the deformation of material blobs initialized along this OECSS, for integration times up to six days. The advection illustrates the existence of a short-term pathway along which initial conditions march towards the bottom right. The deformation of the blobs has a characteristic boomerang shape, which is similar to that observed along persistent Lagrangian jets.<sup>10,14</sup> This objective short-term transport route, therefore, has a clearly verifiable material impact even though it has no clear signature in the instantaneous streamline geometry.

## IX. CONCLUSIONS

We have developed a variational theory of objective Eulerian Coherent Structures (OECSSs) for two-dimensional, non-autonomous dynamical systems. In this theory, we define OECSSs at time  $t$  as curves with the lowest instantaneous material stretching rate or shearing rate in the flow. We defined elliptic OECSSs as closed stationary curves of the instantaneous stretching-rate and shearless OECSSs as stationary curves of the instantaneous shearing-rate functional. A further classification of shearless OECSSs divides them into

hyperbolic (attracting or repelling) and parabolic (jet-type) OECSSs. The approach we have taken here is objective, i.e., returns the same OECSSs in frames translating and rotating relative to each other.

In our present, instantaneous context, objectivity guarantees a self-consistent detection of short-term material coherent structures via OECSSs in unsteady, two-dimensional fluid flows. Indeed, we have shown that an elliptic OECSS provides an accurate identification of short-term material vortices; hyperbolic OECSSs reveal generalized saddle points with the corresponding stable and unstable manifolds; and parabolic OECSSs uncover short-term jet-type pathways for material transport. We have verified the accuracy of these OECSS-based predictions by actual material advection in our ocean data example obtained from satellite altimetry.

We have also compared our results to other broadly used instantaneous coherent structure indicators: streamline topology (which is neither Galilean invariant nor objective) and the Okubo–Weiss criterion (which is Galilean invariant but not objective). Such diagnostics often need an *ad hoc* selection of threshold parameters, which limits the reliability of the results they provide. In contrast, our procedure uses no free parameters or thresholds.

We have found examples of false positives and false negatives suggested by these non-objective Eulerian indicators. For instance, several regions of maximum OW– ellipticity turn out to stretch significantly more than the regions identified by elliptic OECSSs. Even when the indicators happen to suggest an OECSS, the objective variational principles

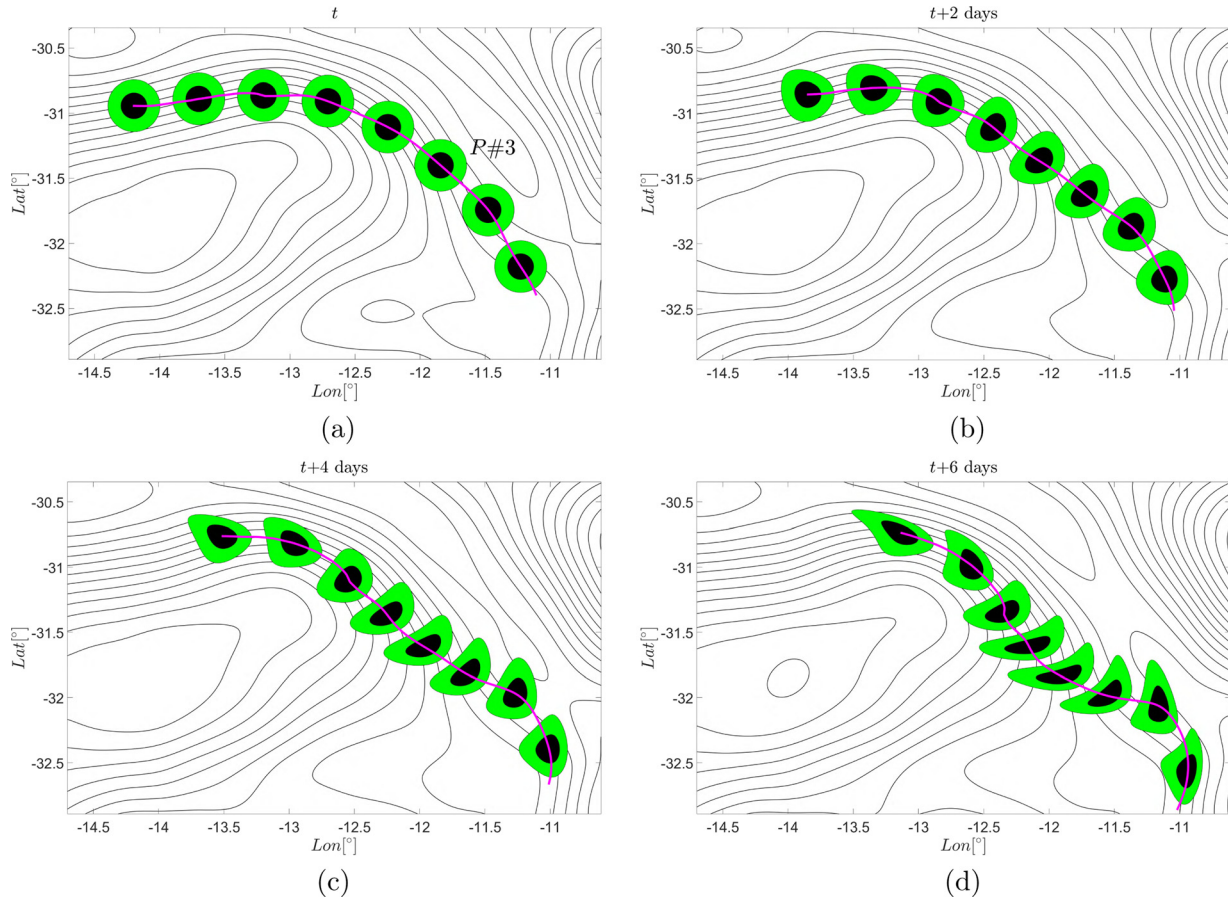


FIG. 16. (a) Parabolic O ECS, P#3, at initial time overlaid on streamlines. (b)–(d) Advected images of the Parabolic O ECS up to 6 days, and its effect on nearby particles. (Multimedia view) [URL: <http://dx.doi.org/10.1063/1.4951720.2>]

developed here give more accurate results, as confirmed by short-term material advection of the detected sets.

As an alternative, elliptic O ECSs can also be sought as closed curves showing short-term rotational coherence, i.e., equal material rotation rate.<sup>19</sup> Obtained as the instantaneous limit of a Lagrangian rotational coherence principle, rotationally coherent O ECSs are also objective. These O ECSs do not restrict stretching rates and hence would generally be expected to give slightly larger but less coherent Eulerian vortices than the ones detected by the approach developed here. Those larger vortices display tangential filamentation, while the stretching-rate-based O ECSs introduced here are instantaneous limits of the perfectly coherent, black-hole-type elliptic LCSs derived in Ref. 18.

O ECS-based forecasting of material transport and mixing is necessarily confined to shorter time scales. Such shorter time scales, however, are precisely the relevant ones for flow control or environmental assessment where quick operational decisions need to be made. Results on the use of O ECSs in short-term forecasting and an extension to higher dimensions will appear elsewhere.

## ACKNOWLEDGMENTS

We would like to acknowledge Mohammad Farazmand for helpful discussions on the subject of this paper.

## APPENDIX A: DEFORMATION-RATE MEASURES FOR MATERIAL CURVES

At time  $t_0$ , consider a smooth curve of initial conditions  $\gamma$ , parametrized as  $s \mapsto x(s)$  via its arclength  $s \in [0, \sigma]$ . Let  $x'(s)$  and  $n(s) = R \frac{x'(s)}{|x'(s)|}$  denote the local tangent and normal vectors to  $\gamma$ , respectively. While tangent vectors of  $\gamma$  are mapped into tangent vectors by the linearized flow map  $\nabla F_{t_0}^t$ , initial normal vectors at time  $t_0$  are not mapped by  $\nabla F_{t_0}^t$  into the normal space at time  $t$  (Fig. 17(a)). The local deformation of  $\gamma$  and its nearby trajectories, over the time interval  $[t_0, t]$ , can be expressed in terms of two Lagrangian quantities: the tangential shear and the tangential strain over the time interval  $[t_0, t]$  (see Refs. 10 and 18).

Specifically, the tangential shear at point  $x(s)$  is given by

$$p_{t_0}^t(s) = D_{t_0}^t(x(s)) = \frac{\langle x'(s), D_{t_0}^t(x(s))x'(s) \rangle}{\sqrt{\langle x'(s), C_{t_0}^t(x(s))x'(s) \rangle \langle x'(s), x'(s) \rangle}},$$

$$D_{t_0}^t := \frac{1}{2} \left[ C_{t_0}^t R - R C_{t_0}^t \right],$$

and the tangential strain at the same point is given by

$$q_{t_0}^t(s) = \frac{\sqrt{\langle x'(s), C_{t_0}^t(x(s))x'(s) \rangle}}{\sqrt{\langle x'(s), x'(s) \rangle}}.$$

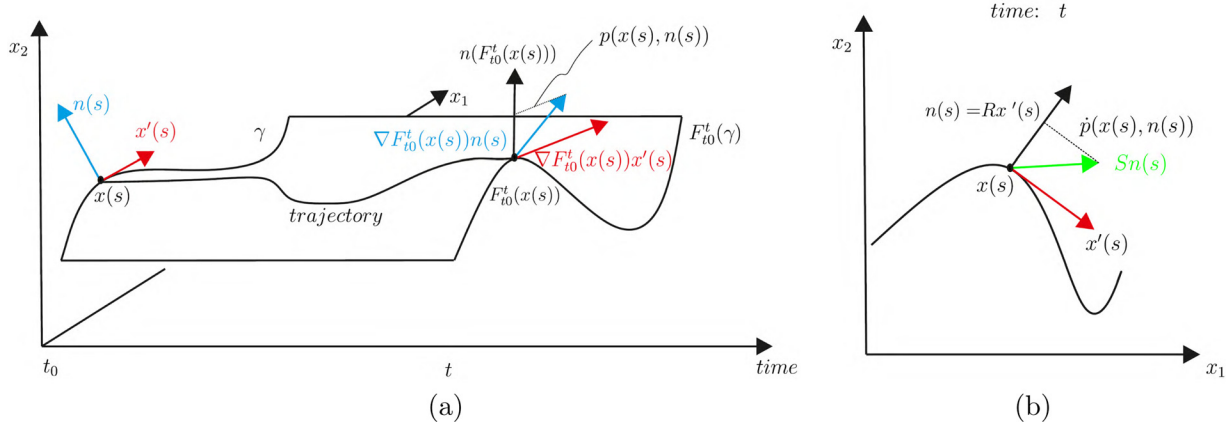


FIG. 17. (a) Evolution of local tangent and normal vectors under the linearized flow map  $\nabla F_{t_0}^t$  in the extended phase space of  $x$  and  $t$ . (b) Eulerian counterpart letting  $x(s)$  be the unit speed parametrization of a regular curve at the current time  $t$ .

The quantities  $p_{t_0}^t$  and  $q_{t_0}^t$  give pointwise information on tangential shear and tangential stretching experienced by a material curve  $\gamma$  over the time interval  $[t_0, t]$  in an objective (frame-invariant) fashion.

The instantaneous rates of shear and tangential stretching along  $\gamma$  can be obtained by differentiating  $p_{t_0}^t$  and  $q_{t_0}^t$  with respect to  $t$  and setting  $t = t_0$ . Specifically, we have

$$\begin{aligned}\dot{p}(s, t) &:= \frac{d}{dt} p_t^{t+\tau}(s)|_{\tau=0} \\ &= \frac{\langle x'(s), [S(x(s), t)R - RS(x(s), t)]x'(s) \rangle}{\langle x'(s), x'(s) \rangle},\end{aligned}$$

and

$$\begin{aligned}\dot{q}(s, t) &:= \frac{d}{d\tau} q_t^{t+\tau}(s)|_{\tau=0} = \frac{1}{\sqrt{\langle x'(s), x'(s) \rangle}} \\ &\quad \times \frac{\langle x'(s), \frac{d}{d\tau} C_t^{t+\tau}(x(s))|_{\tau=0} x'(s) \rangle}{2 \sqrt{\langle x'(s), C_t^t(x(s))x'(s) \rangle}} \\ &= \frac{\langle x'(s), S(x(s), t)x'(s) \rangle}{\langle x'(s), x'(s) \rangle},\end{aligned}$$

where we used the following relations:

$$\begin{aligned}\nabla F_t^t(x) &= I, \quad \frac{d}{d\tau} \nabla F_t^{t+\tau}(x)|_{\tau=0} = \nabla v(x, t) \nabla F_t^t(x) = \nabla v(x, t), \\ \frac{d}{d\tau} C_t^{t+\tau}(x)|_{\tau=0} &= \left( \dot{\nabla} F_t^{t+\tau}(x)^\top \nabla F_t^{t+\tau}(x) + \nabla F_t^{t+\tau}(x)^\top \dot{\nabla} F_t^{t+\tau}(x) \right)|_{\tau=0} = 2S(x, t), \\ \frac{d}{d\tau} D_t^{t+\tau}|_{\tau=0}(x) &= [S(x, t)R - RS(x, t)], \quad D_t^t = 0.\end{aligned}\tag{A1}$$

## APPENDIX B: $\chi_\mu^\pm$ IS A ONE-PARAMETER FAMILY OF ROTATED VECTOR FIELDS

Assume there exists a limit cycle of (16),  $\gamma$ , for one choice of  $\pm$  and a fixed value of  $\mu$ . The hyperbolic nature of limit cycles guarantees their persistence with respect to small changes in the parameter  $\mu$ , which leads to a one-parameter family of limit cycles for the vector field  $\chi_\mu^\pm$ . In general, these limit cycles can deform in an arbitrary fashion and even intersect each other.

In the present case, however,  $\chi_\mu^\pm$  turns out to be as a *one-parameter family of rotated vector fields* in the sense of Ref. 9. This means that trajectories of (16), for each of the choices  $\pm$ , cannot intersect when  $\mu$  varies and shrink or expand for monotonic changes of the parameter. Hence, limit cycles of *one-parameter family of rotated vector fields*,

corresponding to different values of  $\mu$ , cannot intersect each other.

To qualify as a *one-parameter family of rotated vector fields*,  $\chi_\mu^\pm$  must be locally smooth in a neighborhood of the limit cycle, and the vector field defined by  $\frac{d}{d\mu} \chi_\mu^\pm \times \chi_\mu^\pm$  must keep the same orientation with respect to the plane spanned by  $\frac{d}{d\mu} \chi_\mu^\pm$  and  $\chi_\mu^\pm$ .

Indeed,  $\chi_\mu^\pm$  is smoothly orientable in the vicinity of limit cycles, although it is not globally orientable due to the orientational discontinuities of the  $e_i$  fields. For the second condition above, it is equivalent to check that  $\text{sign} \langle \frac{d}{d\mu} \chi_\mu^\pm \times \chi_\mu^\pm, e_3 \rangle$ , with  $e_3$  denoting the planar unit vector, remains unaltered over the domain  $U_\mu$  for each of the choices  $\pm$ .

In the  $[e_1, e_2, e_3]$  basis,  $\langle \frac{d}{d\mu} \chi_\mu^\pm \times \chi_\mu^\pm, e_3 \rangle$  can be computed as

$$O_\mu^\pm(x) = \chi_\mu^\pm \times \frac{d}{d\mu} \chi_\mu^\pm(x) = o_\mu^\pm(x) e_3,$$

$$o_\mu^\pm(x) = \left\langle \frac{d}{d\mu} \chi_\mu^\pm \times \chi_\mu^\pm, e_3 \right\rangle = \frac{\pm}{2\sqrt{(\mu - s_1)(s_2 - \mu)}},$$

therefore,  $\frac{d}{d\mu} \chi_\mu^\pm \times \chi_\mu^\pm$  keeps the same orientation for each of the signs  $\pm$ , under a monotonic change of the parameter  $\mu$ .

With our choice of relative orientation between  $e_1$  and  $e_2$  (cf. Equation (4)), the sign of  $o_\mu^\pm(x)$  gives the direction of rotation (positive counterclockwise) of the  $\chi_\mu^\pm$  field when the parameter  $\mu$  increases, for each of the choices  $\pm$ . Finally, the quantity  $o_\mu^\pm(x)$  could be used in the computation of Elliptic OECs through a systematic change of the parameter  $\mu$ , as described in Ref. 18.

- <sup>1</sup>M. R. Allshouse and J. L. Thiffeault, "Detecting coherent structures using braids," *Physica D* **241**, 95–105 (2012).
- <sup>2</sup>J. K. Beem, P. L. Ehrlich, and L. E. Kevin, *Global Lorentzian Geometry* (CRC Press, 1996).
- <sup>3</sup>F. J. Beron-Vera, Y. Wang, M. J. Olascoaga, G. J. Goni, and G. Haller, "Objective detection of oceanic eddies and the Agulhas leakage," *J. Phys. Oceanogr.* **43**, 1426–1438 (2013).
- <sup>4</sup>G. Boffetta, G. Lacorata, G. Redaelli, and A. Vulpiani, "Detecting barriers to transport: A review of different techniques," *Physica D* **159**, 58–70 (2001).
- <sup>5</sup>M. Budović and I. Mezić, "Geometry of the ergodic quotient reveals coherent structures in flows," *Physica D* **241**, 1255–1269 (2012).
- <sup>6</sup>P. Chakraborty, S. Balachandar, and R. J. Adrian, "On the relationships between local vortex identification schemes," *J. Fluid Mech.* **535**, 189–214 (2005).
- <sup>7</sup>T. Delmarcelle, "The visualization of second-order tensor fields," Ph.D. thesis (Stanford University, CA, 1994).
- <sup>8</sup>T. Delmarcelle and L. Hesslink, "The topology of symmetric, second-order tensor fields," in *Proceedings of the Conference on Visualization'94* (IEEE Computer Society Press, 1994), pp. 140–147.
- <sup>9</sup>G. F. D. Duff, "Limit-cycles and rotated vector fields," *Ann. Math. Second Series* **57**(1), 15–31 (1953).
- <sup>10</sup>M. Farazmand, D. Blazevski, and G. Haller, "Shearless transport barriers in unsteady two-dimensional flows and maps," *Physica D* **278**, 44–57 (2014).
- <sup>11</sup>M. Farazmand and G. Haller, "Computing Lagrangian coherent structures from their variational theory," *Chaos* **22**, 013128 (2012).
- <sup>12</sup>M. Farazmand and G. Haller, "Erratum and addendum to 'A variational theory of hyperbolic Lagrangian coherent structures [Physica D 240, 574–598 (2011)]'," *Physica D* **241**(4), 439–441 (2012).

- <sup>13</sup>G. Froyland and K. Padberg-Gehle, "Almost-invariant and finite-time coherent sets: Directionality, duration, and diffusion," in *Ergodic Theory, Open Dynamics, and Coherent Structures* (Springer, 2014), pp. 171–216.
- <sup>14</sup>A. Hadjighasem and G. Haller, "Geodesic transport barriers in Jupiter's atmosphere: A video-based analysis," *SIAM Rev.* **58**(1), 69–89 (2016).
- <sup>15</sup>G. Haller, "An objective definition of a vortex," *J. Fluid Mech.* **525**, 1–26 (2005).
- <sup>16</sup>G. Haller, "A variational theory of hyperbolic Lagrangian coherent structures," *Physica D* **240**, 574–598 (2011).
- <sup>17</sup>G. Haller, "Lagrangian coherent structures," *Annual Rev. Fluid. Mech.* **47**, 137–162 (2015).
- <sup>18</sup>G. Haller and F. J. Beron-Vera, "Coherent Lagrangian vortices: The black holes of turbulence," *J. Fluid Mech.* **731**, 9 (2013).
- <sup>19</sup>G. Haller, A. Hadjighasem, M. Farazmand, and F. Huhn, "Defining coherent vortices objectively from the vorticity," *J. Fluid Mech.* **795**, 136–173 (2016).
- <sup>20</sup>G. Haller and A. Poje, "Finite time transport in aperiodic flows," *Physica D* **119**, 352–380 (1998).
- <sup>21</sup>J. Jeong and F. Hussain, "On the identification of a vortex," *J. Fluid Mech.* **285**, 69–94 (1995).
- <sup>22</sup>D. Karrasch, F. Huhn, and G. Haller, "Automated detection of coherent Lagrangian vortices in two-dimensional unsteady flows," in *Proc. R. Soc. London A* **471**, 2173 (2015).
- <sup>23</sup>G. Lapeyre, B. L. Hua, and B. Legras, "Comment on 'Finding finite-time invariant manifolds in two-dimensional velocity fields,'" *Chaos* **11**, 427–430 (2001).
- <sup>24</sup>G. Lapeyre, P. Klein, and B. L. Hua, "Does the tracer gradient vector align with the strain eigenvectors in 2D turbulence?," *Phys. Fluids* **11**, 3729–3737 (1999).
- <sup>25</sup>H. J. Lugt, "The dilemma of defining a vortex," in *Recent Developments in Theoretical and Experimental Fluid Mechanics* (Springer, 1979), pp. 309–321.
- <sup>26</sup>T. Ma and E. M. Boltt, "Differential geometry perspective of shape coherence and curvature evolution by finite-time nonhyperbolic splitting," *SIAM J. Appl. Dyn. Syst.* **13**, 1106–1136 (2014).
- <sup>27</sup>A. Okubo, "Horizontal dispersion of floatable particles in the vicinity of velocity singularities such as convergences," in *Deep-Sea Research* (Elsevier, 1970), Vol. 17, pp. 445–454.
- <sup>28</sup>T. Peacock and J. Dabiri, "Introduction to focus issue: Lagrangian coherent structures," *Chaos* **20**, 017501 (2010).
- <sup>29</sup>T. Peacock, G. Froyland, and G. Haller, "Introduction to focus issue: Objective detection of coherent structures," *Chaos* **25**, 087201–087201 (2015).
- <sup>30</sup>A. Provenzale, "Transport by coherent barotropic vortices," *Annual Rev. Fluid. Mech.* **31**, 55–93 (1999).
- <sup>31</sup>M. Tabor and I. Klapper, "Stretching and alignment in chaotic and turbulent flows," *Chaos, Solitons Fractals* **4**, 1031–1055 (1994).
- <sup>32</sup>C. Truesdell and W. Noll, *The Non-Linear Field Theories of Mechanics* (Springer, 2004).
- <sup>33</sup>J. Weiss, "The dynamics of enstrophy transfer in two-dimensional hydrodynamics," *Physica D* **48**, 273–294 (1991).